Journal of Materials Chemistry B

ROYAL SOCIETY OF CHEMISTRY

PAPER

View Article Online
View Journal | View Issue

Cite this: J. Mater. Chem. B, 2024, 12, 2771

Synergy between 3D-extruded electroconductive scaffolds and electrical stimulation to improve bone tissue engineering strategies†

João C. Silva, ‡*[abc] Pedro Marcelino, [abcd] João Meneses, [d] Frederico Barbosa, [abc] Carla S. Moura, [de] Ana C. Marques, [fg] Joaquim M. S. Cabral, [abc] Paula Pascoal-Faria, [dhj] Nuno Alves, [dij] Jorge Morgado, [ck] Frederico Castelo Ferreira *[abc] and Fábio F. F. Garrudo ‡*[abck]

In this work, we propose a simple, reliable, and versatile strategy to create 3D electroconductive scaffolds suitable for bone tissue engineering (TE) applications with electrical stimulation (ES). The proposed scaffolds are made of 3D-extruded poly(ε-caprolactone) (PCL), subjected to alkaline treatment, and of poly(3,4-ethylenedioxythiophene):poly(styrene sulfonate) (PEDOT:PSS), anchored to PCL with one of two different crosslinkers: (3-glycidyloxypropyl)trimethoxysilane (GOPS) and divinyl sulfone (DVS). Both cross-linkers allowed the formation of a homogenous and continuous coating of PEDOT:PSS to PCL. We show that these PEDOT:PSS coatings are electroconductive (11.3–20.1 S cm^{-1}), stable (up to 21 days in saline solution), and allow the immobilization of gelatin (Gel) to further improve bioactivity. *In vitro* mineralization of the corresponding 3D conductive scaffolds was greatly enhanced (GOPS(NaOH)-Gel – 3.1 fold, DVS(NaOH)-Gel – 2.0 fold) and cell colonization and proliferation were the highest for the DVS(NaOH)-Gel scaffold. *In silico* modelling of ES application in DVS(NaOH)-Gel scaffolds indicates that the electrical field distribution is homogeneous, which reduces the probability of formation of faradaic products. Osteogenic differentiation of human bone marrow derived mesenchymal stem/stromal cells (hBM-MSCs) was performed under ES. Importantly, our results clearly demonstrated a synergistic effect of scaffold electroconductivity and ES on the enhancement of MSC osteogenic differentiation, particularly on cell-secreted calcium deposition and the upregulation of osteogenic gene markers such as *COL I*, *OC* and *CACNA1C*. These scaffolds hold promise for future clinical applications, including manufacturing of personalized bone TE grafts for transplantation with enhanced maturation/functionality or bioelectronic devices.

Received 10th November 2023,
Accepted 2nd February 2024

DOI: 10.1039/d3tb02673f

rsc.li/materials-b

[a] iBB – Institute for Bioengineering and Biosciences, Instituto Superior Técnico, Universidade de Lisboa, Av. Rovisco Pais, Lisboa 1049-001, Portugal. E-mail: joao.f.da.silva@tecnico.ulisboa.pt, frederico.ferreira@tecnico.ulisboa.pt, fabio.garrudo@tecnico.ulisboa.pt, fabio.garrudo@edu.ulisboa.pt
[b] Associate Laboratory i4HB – Institute for Health and Bioeconomy, Avenida. Rovisco Pais, Lisboa 1049-001, Portugal
[c] Department of Bioengineering, Instituto Superior Técnico, Universidade de Lisboa, Avenida Rovisco Pais, Lisboa 1049-001, Portugal
[d] CDRSP – Centre for Rapid and Sustainable Product Development, Polytechnic Institute of Leiria, Rua de Portugal-Zona Industrial, Marinha Grande 2430-028, Portugal
[e] Research Centre for Natural Resources Environment and Society (CERNAS), Polytechnic Institute of Coimbra, Bencanta, 3045-601 Coimbra, Portugal
[f] CERENA, DEQ, Instituto Superior Técnico, Universidade de Lisboa, Avenida Rovisco Pais, Lisboa 1049-001, Portugal
[g] Department of Chemical Engineering, Instituto Superior Técnico, Universidade de Lisboa, Avenida Rovisco Pais, Lisboa 1049-001, Portugal
[h] Department of Mathematics, School of Technology and Management, Polytechnic of Leiria, Morro do Lena—Alto do Vieiro, Apartado 4163, Leiria 2411-901, Portugal
[i] Department of Mechanical Engineering, School of Technology and Management, Polytechnic of Leiria, Morro do Lena—Alto do Vieiro, Apartado 4163, Leiria 2411-901, Portugal
[j] Associate Laboratory Arise, Porto, Portugal
[k] Instituto de Telecomunicações, Instituto Superior Técnico, Universidade de Lisboa, Avenida Rovisco Pais, Lisboa 1049-001, Portugal

† Electronic supplementary information (ESI) available. See DOI: https://doi.org/10.1039/d3tb02673f

‡ These authors contributed equally to this work.

1. Introduction

Bone diseases are both the cause and a side-effect of several chronic diseases and iatrogenicity that greatly affects the elderly. Osteoporosis, meaning ''porous bone'', is one of such diseases. It is a global disease whose prevalence and economic burden will increase with the aging of the world population, affecting severely diverse geographical areas such as Europe, the USA and China. Kanis and colleagues[1] reported the prevalence of osteoporosis in the combined entire population of the European Union, United Kingdom, and Switzerland (EU27 + 2) to be 5.6% (32 million individuals). The total cost of osteoporosis in EU27 + 2, including direct costs (64%), ongoing costs (33%), and cost of pharmacological intervention (3%), was around €56.9 Billion in 2019. If such an amount was directly supported by the EU, it would correspond to approximately 42% of its 2019 total budget. Osteoporosis ultimately arises from a predominance of bone resorption over deposition (loss of bone mass), leading to bone fragility and susceptibility to fracture.[2] Diverse pharmacological strategies have been designed to treat osteoporosis, but these fail in reverting its progression.[3,4] Moreover, even when considering heathy bone, the ability to self-regenerate is impaired by critical fracture sizes, a phenomena seen for example in non-unions, which represents approximately 5–10% of all acute fractures reported.[5] As such, there is a need for new therapeutic approaches targeting osteoporosis and non-union fractures with potential long-lasting positive effects on bone tissue regeneration.

Electrical stimulation (ES) is a powerful tool with potential therapeutic application in bone diseases.[6] Fonseca Junior and colleagues[7] reported the benefit of combining ES (10 μA) with commercial bone grafts to reduce inflammation and improve vascularization and mineralization in transplanted rats. Leppik and colleagues[8] observed, in rats, an enhancement on new bone formation, increased vascularization and improvement of the mechanical properties when ES (0.1–0.2 μA) was used concomitantly with transplanted mesenchymal stem/stromal cells (MSCs) cultured on β-tricalcium phosphate granules. The authors also showed that ES (1 V cm^{-1}, 1 h day^{-1}, and 21 days) could greatly enhance the osteogenic differentiation of rat MSCs. In a follow-up study, Oliveira and colleagues[9] observed that ES promoted tissue healing over scarring in amputated rats. This was attributed to ES induced anisotropy of collagen fibers, and promotion of short-term inflammation and long-term cell proliferation. Additionally, other *in vitro* studies support these observations.[10–13] Overall, the use of ES holds high promise for innovative tissue engineering (TE) strategies targeting the repair of osteoporosis-related non-union fractures.

Additive manufacturing technologies enable the fabrication of electroactive constructs with complex architectures both for TE applications and to be used as soft electronics devices for man–machine interfaces.[14,15] 3D-melt extrusion or fused deposition modeling (FDM) is an additive manufacturing technique that uses thermoplastics, such as poly(ε-caprolactone) (PCL), to create scaffolds that structurally and mechanically mimic the bone tissue.[16–18] PCL is an FDA-approved polymer for biomedical products and a first choice for scaffold development for bone TE applications.[19] This is due to its biocompatibility, advantageous mechanical properties to support bone tissue and tunable degradation profile.[19,20] Our group has previously developed 3D PCL scaffolds with high porosity and interconnectivity, and capable of supporting MSC growth and chondrogenic differentiation.[21,22] These can also be used for bone repair applications due to their controlled architecture, high porosity/pore size and ease of functionalization. We and other groups had also showed the successful inclusion of bioactive components such as hydroxyapatite,[23] β-tricalcium phosphate,[24] fibrin[25] and deposited MSC-derived ECMs[26] to greatly increase their osteogenic potential. However, PCL-derived scaffolds are not suitable for effectively harnessing ES to cultured cells and thus require further modifications.

Electroconductive polymers (ECPs) can be used to fabricate electroactive scaffolds for TE strategies. ECPs present important advantages for overall TE applications, including effective ES of stem cells, design of impedance sensors to monitor cell health and ES-controlled drug release.[27–29] ECPs cannot be easily printed/extruded in 3D structures due to the absence of a melting point compatible with the manufacturing process. Thus, they require advanced processing and specialized additive manufacturing techniques[15,30] and/or the development of polymer blends with reduced electroconductivity.[31–33] Poly(3,4-ethylenedioxythiophene):poly(styrene sulfonate) (PEDOT:PSS) is an ECP, suitable for the design of TE scaffolds due to its high stability and biocompatibility.[34–36] For example, Guex and colleagues[37] reported the development of an electroconductive (6.1×10^{-6} S cm^{-1}) ice-templated PEDOT:PSS scaffold capable of supporting MC3T3-E1 cells' osteogenic differentiation and the deposition of the mineralized extracellular matrix (ECM). PEDOT:PSS can also be processed into versatile electroconductive composites with collagen[38] and nanohydroxyapatite/chitosan[39] for bone TE applications. Nevertheless, its inclusion in composites suitable for 3D-extrusion remains limited.

In our previous work, we studied the performance of PEDOT:PSS films, cross-linked using (3-glycidyloxypropyl)-trimethoxysilane (GOPS) and divinyl sulfone (DVS), for neural applications.[40] The chemistry involved in the cross-linking of PEDOT:PSS with GOPS/DVS involves the formation of ether/ester bonds with PSS and the respective support substrate (*e.g.* glass). We hypothesize that cross-linked PEDOT:PSS can be used to homogeneously coat 3D-extruded scaffolds made of polyesters (*e.g.* PCL), widely used in biomedical applications.[19] The presence of free hydroxyl/carbonyl groups, maximized through alkaline treatment, ensures effective immobilization of PEDOT:PSS at their surface and the formation of continuous films. This potential strategy is easy, straightforward and can be used with scaffolds with diverse architecture without the need for specialized equipment.

The goal of this work is to create an electroconductive 3D scaffold suitable for bone tissue engineering and electrical stimulation using a simple, reliable, and versatile method,

based on the combination of 2D and 3D materials.[41] The envisaged scaffold is composed of a 3D-extruded PCL skeleton and a cross-linked PEDOT:PSS coating. We harnessed the chemistry of both materials, and later in combination with gelatin, to create a stable yet bioactive and mechanically robust scaffold. We used *in silico* tools to further demonstrate the advantages of a PEDOT:SS coating on electrical field distribution in a porous scaffold. Finally, we used the best PCL-PEDOT:PSS scaffold combination to study its ability to enhance osteogenic differentiation of MSCs under electrical stimulation. The design and production strategy employed are highly versatile and easy to implement on similar scaffolds with different architectures. We believe that this strategy can be used in future clinical applications, including transplantation of personalized bone TE constructs with enhanced maturation/functionality or devices for bioelectronic applications.

2. Experimental section

2.1. Materials

Di-potassium hydrogen phosphate trihydrate was supplied by AppliChem GmbH (Darmstadt, Germany). Medical glue (silastic® medical adhesive silicone type A) was obtained from Biesterfeld Spezialchemie Ibérica, S.L.U. (Barcelona, Spain). Alkaline phosphatase (ALP) assay kits were supplied by BioAssay Systems (Hayward, CA, USA). Magnesium chloride hexahydrate was supplied by Fagron (Rotterdam, The Netherlands). Hydrochloric acid 37% and sodium hydrogen carbonate were supplied by Fisher Scientific (Hampton, NH, USA). PEDOT:PSS dispersion Clevios™ PH 1000 (PEDOT : PSS ratio of 1 : 2.5, solids content 1.0–1.3%) was supplied by Heraeus (Hanau, Germany). Anhydrous calcium chloride was supplied by Honeywell International Inc. (Charlotte, NC, USA). PCL flexible filament (1.75 mm) was supplied by Makerbot (New York City, NY, USA). qPCR NZYSpeedy green master mix (2×) ROX plus was supplied by NZYTech (Lisboa, Portugal). RNA extraction kit RNeasy Mini was supplied by Qiagen (Hilden, Germany). 2-Phospho-L-ascorbic acid, (3-glycidyloxypropyl)trimethoxysilane (GOPS), 4,6-diamidino-2-phenylindole dihydrochloride (DAPI), β-glycerophosphate, calcium colorimetric assay kit, dexamethasone, divinyl sulfone (DVS), dodecylbenzenesulfonic acid (DBSA), anhydrous ethylene glycol (EG), gelatin from porcine skin (type A, gel strength 300) (Gel), hexamethyldisilazane (HMDS), paraformaldehyde (PFA) phalloidin-TRITC (2 μg mL^{-1} in PBS), potassium chloride, sodium chloride, sodium hydroxide, anhydrous sodium sulfate, SYLGARD® 184 silicone elastomer (poly(dimethylsiloxane)), and xylenol orange solution were supplied by Sigma-Aldrich (St. Louis, MO-IL, USA). Antibiotic–antimycotic (Anti–Anti) mixture, antibodies anti-type I collagen (MA1-26771), anti-osteopontin (MA5-17180), anti-mouse AlexaFluor 488, Dulbecco's phosphate buffer saline (PBS), Dulbecco's modified Eagle's medium (DMEM), MSC-qualified fetal bovine serum (FBS), Pen-Strep mixture (penicillin 10 000 units mL^{-1}, streptomycin 10 000 μg mL^{-1}), High-capacity cDNA reverse transcription kits, MicroAmp Fast Optical 96-well reaction plates, reazurin (AlamarBlue™ cell viability reagent), and Triton-X-100 (SurfactAmps®, 10% in water) were supplied by Thermofisher Scientific (Waltham, MA, USA).

2.2. 3D Extrusion printing of PCL constructs

PCL constructs (films and scaffolds) were designed using the computer-aided design (CAD) software Autodesk Fusion 360 (version up to 2.0.11415, Autodesk, Inc., San Francisco, CA, USA). The models designed were exported as STL files by FDM to a Prusa i3 MK3S commercial 3D printer (Prusa Research, Praha, Czech Republic). Slicing of the STL files into G-code was done in PrusaSlicer 2.3.1 (Prusa Research). For 3D printing, nozzle (brass, 0.25 mm in diameter – Prusa Research) and bed temperatures were set to 95 °C and 40 °C, respectively. The layer height was defined as 0.15 mm for all layers, and the default "Quality" profile was adopted for printing.

The designed PCL film was shaped as a 20 mm × 10 mm × 0.5 mm cuboid. To fill any gaps and ensure a smooth first layer, the first layer was modified to be printed with a 0.15 mm extrusion width and using a 1.2 extrusion multiplier.

For the PCL scaffold design, an orthogonal pattern with aligned fibers was chosen (0–90° rotations between successive layers). The pore size of the scaffold and fiber diameter were both specified to have a dimension of 300 μm. The overall scaffold size was 10.5 mm × 10.5 mm × 3 mm. Since each scaffold layer had a height of 0.30 mm with the defined printing layer height of 0.15 mm, two printing passages were necessary to print each scaffold layer.

2.3. PEDOT:PSS coatings of PCL constructs

Following previous work by Moura and colleagues,[22] pristine PCL constructs (films and scaffolds) were incubated in an aqueous solution of NaOH (1 M) for 24 hours to improve hydrophilicity (PCL(NaOH)).

PCL and PCL(NaOH) scaffolds were coated with PEDOT:PSS to become electroconductive. For this, four different PEDOT:PSS solutions were prepared for the dip-coating of the scaffolds:

Solution 1: PEDOT : PSS + EG (1 : 4, by volume) + DBSA (0.5 μL mL^{-1}) + GOPS (10 μL mL^{-1}), followed by overnight agitation.

Solution 2: content of solution 1 + gelatin (2%, by weight with respect to the PEDOT:PSS volume used), followed by overnight agitation and 50 °C.

Solution 3: PEDOT : PSS + EG (1 : 4, by volume) + DBSA (0.5 μL mL^{-1}) + DVS (30 μL mL^{-1}), followed by overnight agitation.

Solution 4: content of solution 3 + gelatin (2%, by weight with respect to the PEDOT:PSS volume used), followed by overnight agitation and 50 °C.

The constructs were submerged in the solutions for 24 hours under constant agitation. These were then collected and annealed at ≈55 °C overnight The chemical formulas of the main components of our scaffolds are depicted in Fig. 1 The summary of the procedure is depicted in Fig. 2. A list of all the samples produced is presented in Table 1.

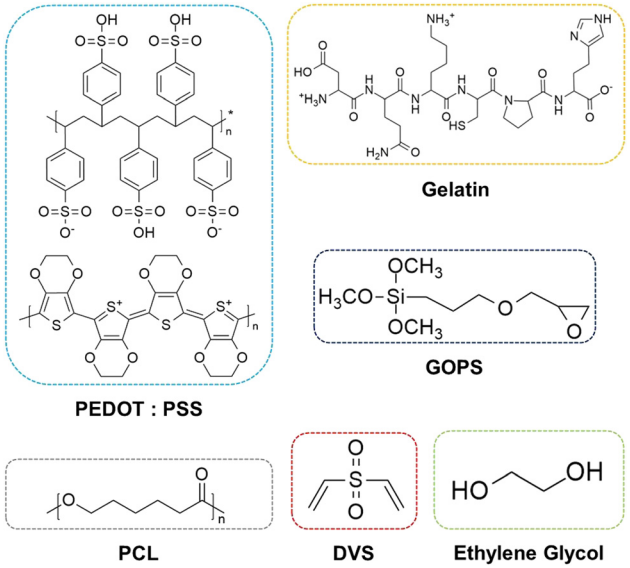

Fig. 1 Chemical formulas of the compounds used in the design of PCL-PEDOT:PSS scaffolds.

2.3.1. Chemical treatment of PCL scaffolds. PCL scaffolds were also subjected to specific chemical treatments to study the effect of temperature (50 °C – cross-linking) and different pH values (2.0 for PEDOT:PSS and 14.0 for the NaOH treatment) on their properties. The conditions are summarized in Table 1 and were the following: incubation at 50 °C for 24 h (50 °C), incubation in 0.05 M H_2SO_4 solution for 24 h (H_2SO_4), and/or incubation in 1 M NaOH solution for 24 h (NaOH).

2.3.2. Production of PEDOT:PSS spin-coated films on glass. PEDOT:PSS spin-coated films were produced (1000 rpm for 12 s, followed by 1500 rpm for 45 s) from solutions 1 (fGOPS), 2 (fGOPS-Gel), 3 (fDVS) and 4 (fDVS-Gel) used for PCL construct coating. The samples were dried at 125 °C and analyzed without further processing.

2.4. Morphological and physico-chemical characterization

2.4.1. Scanning electron microscopy (SEM). The surface morphology of extruded PCL and PCL-PEDOT:PSS constructs was evaluated using a Hitachi S-2400 SEM (Hitachi, Chiyoda, Tokyo, Japan) at 20 kV, after coating with a thin layer of gold/palladium.

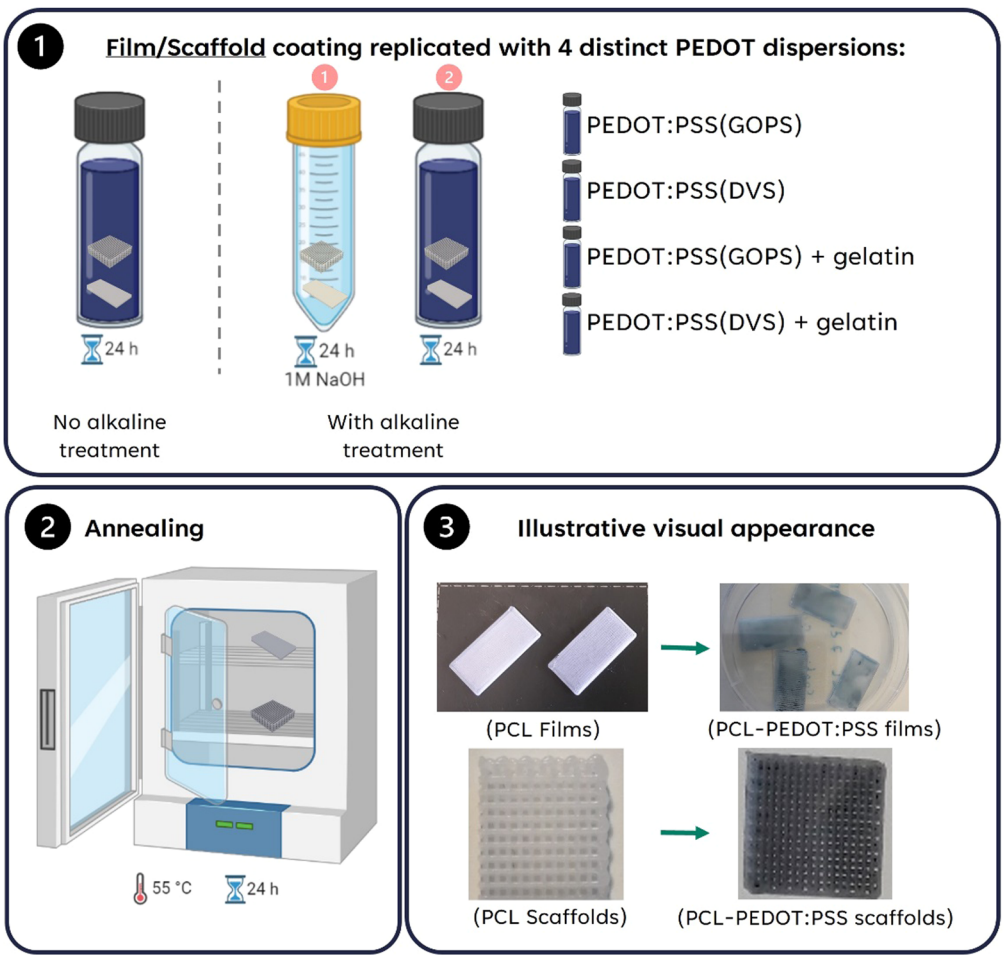

Fig. 2 Summary of the protocols used to coat PCL films/scaffolds and respective PEDOT:PSS solutions used (Image created using BioRender.com, agreement number: OY26H1R3WS).

Table 1 Summary of the samples produced, composition of the coating solutions, and annealing treatments

		PEDOT:PSS solution used for coating						
Sample code	NaOH treatment	EG ($V\ V^{-1}$)	DBSA (0.5 $\mu L\ mL^{-1}$)	GOPS ($\mu L\ mL^{-1}$)	DVS ($\mu L\ mL^{-1}$)	Gelatin (% m V^{-1})	H_2SO_4 treatment	Annealing at 50 °C
PCL	No	X	X	X	X	X	X	No
PCL(NaOH)	Yes	X	X	X	X	X	X	No
GOPS	No	1 : 4	0.5	10	X	X	X	Yes
GOPS(NaOH)	Yes	1 : 4	0.5	10	X	X	X	Yes
GOPS(NaOH)-Gel	Yes	1 : 4	0.5	10	X	2	X	Yes
DVS	No	1 : 4	0.5	X	30	X	X	Yes
DVS(NaOH)	Yes	1 : 4	0.5	X	30	X	X	Yes
DVS(NaOH)-Gel	Yes	1 : 4	0.5	X	30	2	X	Yes
PCL(50 °C)	No	X	X	X	X	X	No	Yes
PCL(H_2SO_4) (50 °C)	No	X	X	X	X	X	Yes	Yes
PCL(NaOH) (50 °C)	Yes	X	X	X	X	X	No	Yes
PCL(NaOH) (H_2SO_4, 50 °C)	Yes	X	X	X	X	X	Yes	Yes

2.4.2. Micro-computed tomography (μCT) imaging. μCT was performed using a SkyScan 1174v2 (Bruker software version 1.1, Bruker, Billerica, MA, USA) to analyze the internal microstructure of the scaffolds. The following scanning parameters were used: a source voltage of 50 kV, a source current of 800 mA, an image pixel size of 14.01 μm, an exposure time of 4000–6000 ms, a rotation step of 0.5–0.6°, no filter, and frame averaging on (2).

Image reconstruction was done using NRecon software, version 1.7.4.6 (Bruker, Billerica, MA, USA). Realistic visualizations of the scaffolds were achieved using CTVox software (version 3.3.1., Bruker, Billerica, MA, USA). Porosity, interconnectivity, and the surface area to volume ratio were directly obtained from the software.

Reconstruction/shape fidelity analysis was performed using CTAn software (version 1.20.0, Bruker, Billerica, MA, USA). The pore size and fiber diameter were obtained from two perpendicular directions for the printed scaffolds: one along the printed layers, and another across the printed layers. Three measurements were made in each direction to obtain the average dimensions.

2.4.3. Attenuated total reflectance-Fourier-transform infrared spectroscopy (ATR-FTIR). The obtained samples were analyzed by ATR-FTIR using a Spectrum Two FT-IR Spectrometer (PerkinElmer, Waltham, MA, USA), equipped with a Pike Technologies MIRacle® ATR accessory. Transmittance spectra were obtained from 400 to 4000 cm^{-1} (resolution of 4 cm^{-1}, accumulation of 8 scans) at room temperature and an automatic baseline correction treatment was applied using the acquisition software. The obtained spectra were normalized to the maximum peak obtained.

2.4.4. Contact angle. Determination of the contact angle of the PCL and PCL-PEDOT:PSS extruded films was performed with a Krüss DSA25B goniometer (Krüss GmbH, Hamburg, Germany) using the sessile drop technique (deionized water). The spreading of the droplet on the extruded films was assessed by measuring the contact angle of the droplet with the surface (n = 6). Drop Shape Analysis 4 Software was employed to take measurements of the left and right angles every 0.5 s for a total time of 1 min.

2.4.5. 4-Point probe electroconductivity measurement. The electroconductivity of PCL-PEDOT:PSS extruded films and PEDOT:PSS spin-coated films was determined using the 4-point probe technique. Four parallel 50 nm thick gold stripes were deposited using a thermal evaporation system Edwards Coating System E 306A (Edwards, Irvine, CA, USA) to improve the electrical contact between the samples (PCL- and PCL-PEDOT:PSS extruded films) and the probes of the measurement/sensing equipment. The electroconductivity of three different films (n = 3) was measured by the four-point probe method, using a current source Keithley DC power source (Keithley Instruments, Cleveland, OH, USA) and an Agilent 34401A multimeter (Agilent Technologies, Santa Clara, CA, USA). The thickness of the PEDOT:PSS layer was measured using a Veeco Dektak 8 Profilometer (Bruker, Billerica, MS, USA).

2.4.6. UV-Visible (UV/Vis) and near-infrared (NIR) spectroscopy. UV/Vis absorption spectra of spin-coated PEDOT:PSS films were obtained with a V-730 UV-Visible spectrophotometer (Jasco, Easton, MD, USA) in the 200–1100 nm range (resolution of 0.2 nm). NIR absorption spectra were obtained using a SPEC NIR 2.4 spectrometer (Sarspec, Vila Nova de Gaia, Portugal) in the 900–2400 nm range. The obtained spectra were normalized to the maximum peak found in the 225–235 nm region.

2.5. Stability assay

The stability of the PCL-PEDOT:PSS films was evaluated in PBS. Briefly, specimens (20 mm × 10 mm × 0.5 mm, n = 5) were incubated with sterile PBS (37 °C, 5% CO_2) for 1, 7, 14 and 21 days. The collected samples were washed with distilled water three times and then dried before initial weighting. Next, the samples were dried at 45 °C for at least 24 h. Film stability was evaluated through FTIR analysis and electroconductivity measurements (Section 2.4.4.).

2.6. Mechanical properties

The mechanical properties of PCL and PCL-PEDOT:PSS scaffolds were evaluated under compression uniaxial testing (1 mm min^{-1}) using a TA.XTplusC Texture Analyser (Stable Micro Systems, Godalming, Surrey, United Kingdom) equipped

with a 50 kg (≈490 N) load cell. For each condition, 5 specimens were tested (n = 5). The obtained data were processed using Connect software (Stable Micro Systems, Godalming, Surrey, United Kingdom). The compressive modulus was determined by calculating the slope of the initial (10–15%) linear region of the stress–strain curves. The ultimate strength was calculated from the maximum of the stress–strain curves when yielding was observed.

2.7. Finite element analysis (FEA) of electrical fields in PCL-PEDOT:PSS scaffolds

Finite element analysis models of the PCL-PEDOT:PSS scaffolds were constructed and solved with the AC/DC module of COMSOL Multiphysics (version 5.2a, www.comsol.com, Stockholm, Sweden).

In model 1, the electrical properties of each fiber were predicted using a single 2D filament model. This procedure was aimed at understanding the impact on the numerical predictions when considering (1) a homogeneous thin electroconductive coating on an inert filament core or (2) the whole electroconductive filament.

In model 2, a 3D complete model of one culture well with an orthogonal scaffold (in permanent contact with both electrodes) was used to compare the predicted electrical field among the different coating material options. This is possible since by construction the electric current that passes through one well is equal to that through the remaining wells placed in series. The electrical current (ec) physics interface was selected, considering a stationary study and applying a floating potential boundary condition at one electrode side surface. The remaining electrode has a ground reference boundary condition. The required electric current and potential measurements were performed with a multimeter (ISO-TECH IDM 73). 3D physics-controlled meshes were also generated in COMSOL. Whole model meshes were constructed using tetrahedra, triangles, edges and vertex with a total of 2.3 million elements. A finite element mesh study was also performed to guarantee that the results, (*i.e.*, minimum element quality: 0.03; average element quality: 0.66; element volume ratio: 9.14×10^{-6}), are independent of the mesh size. The properties of the materials used in FEA are described in Table S1 (ESI†). The COMSOL linear stationary iterative solver was used to compute the solution for each model.

2.8. Mineralization assay

The *in vivo* bone bioactivity of the scaffolds was simulated by incubating the 3D printed scaffolds in simulated body fluid (SBF). SBF was prepared according to a protocol described by Kokubo and Takadama[42] and the final ionic concentrations obtained were: Na^+ (142.0 mM), K^+ (5.0 mM), Mg^{2+} (1.5 mM), Ca^{2+} (2.5 mM), Cl^- (147.8 mM), HCO_3^- (4.2 mM), HPO_4^{2-} (1.0 mM), and SO_4^{2-} (0.5 mM). Prior to incubation, the scaffolds were washed with ethanol (20%, w/v) and distilled water. Scaffolds were incubated in SBF at 37 °C for 21 days, with SBF exchanged every 2 days. At the end, scaffolds were then thoroughly washed with Mili-Q® water and dried overnight at 45 °C. SEM (Section 2.4.1.) was used to evaluate the presence of minerals on the different experimental groups. Additionally, the amount of calcium deposited on each scaffold was quantified using a calcium colorimetric assay (Section 2.13.4).

2.9. Human mesenchymal stem/stromal cell culture

Human bone marrow-derived mesenchymal stem/stromal cells (hBM-MSCs) used were part of the cell bank available at the Stem Cell Engineering Research Group (SCERG) from the Institute for Bioengineering and Biosciences (iBB) at Instituto Superior Técnico-Universidade de Lisboa. hBM-MSCs were isolated according to protocols previously established at iBB.[43] Bone marrow aspirates (Male 46 years) were obtained from Centro Clínico da Guarda Nacional Republicana (GNR), Lisboa, under the framework of ongoing collaboration agreements with iBB. All human samples were obtained from healthy donors after written informed consent according to Directive 2004/23/EC of the European Parliament and of the Council of March 31, 2004, on setting standards of quality and safety for the donation, procurement, testing, processing, preservation, storage, and distribution of human tissues and cells (Portuguese Law 22/2007, June 29), with the approval of the Ethics Committee of the respective clinical institution. Isolated hBM-MSCs were kept frozen in liquid/vapor nitrogen tanks until further use. Prior to the *in vitro* culture assays, the hBM-MSCs were thawed and expanded on tissue culture flasks (T-75 cm2) using low-glucose DMEM supplemented with 10% FBS (MSC qualified) and 1% Anti–Anti. The cells were cultured in an incubator at 37 °C and 5% CO_2 in a humidified atmosphere and the medium was fully renewed every 2–3 days. All the experimental assays were performed using hBM-MSCs between passages 3 and 5.

2.10. Assessment of hBM-MSC proliferation and morphology using different PCL-PEDOT scaffolds

Before seeding the cells, the different scaffolds were sterilized by exposure to ultraviolet (UV) radiation (2 h each side of the scaffold), followed by rinsing three times with a 1% Anti–Anti solution (in PBS) for 3 h. Afterwards, the scaffolds were incubated with culture media for 1 h at 37 °C and 5% CO_2.

The hBM-MSCs were seeded on the scaffolds at a density of 120 000 cells per scaffold. The cell-seeded scaffolds were incubated at 37 °C and 5% CO_2 in a humidified atmosphere for 2 h without cell culture medium to promote initial cell adhesion. The cultures were maintained for 7 days under standard expansion medium (DMEM + 10% FBS (MSC qualified) + 1% Anti–Anti) in an incubator at 37 °C and 5% CO_2 and the medium was replaced every 2–3 days.

The proliferation of hBM-MSCs on the different scaffold conditions was monitored on days 1, 4 and 7 using the AlamarBlue™ assay following the manufacturer's guidelines. Briefly, a 10% (v/v) AlamarBlue™ solution diluted in cell culture medium was added to the scaffolds and incubated at 37 °C and 5% CO_2 in a humidified atmosphere for 3 h. The fluorescence intensity values were measured in a microplate reader (Infinite 200 Pro; Tecan, Switzerland) at an excitation/emission

wavelength of 560/590 nm. For each experimental group, the fluorescence intensity was analyzed for four independent scaffolds ($n = 4$) and acellular scaffolds were used as blank controls.

In order to evaluate the morphology of hBM-MSCs on the different scaffolds, samples were stained with DAPI (1.5 μg mL^{-1} in PBS) and Phalloidin-TRITC (2 μg mL^{-1} in PBS). The cells were first washed with PBS and fixed with a 4% PFA solution for 10 min. Afterwards, cells were incubated with blocking solution (10% goat serum and 0.2% Triton-X-100 in PBS) for 30 min. Samples were then incubated with Phalloidin-TRITC for 45 min in the dark. After this, the samples were washed twice with PBS and counterstained with DAPI for 5 min. Finally, the samples were washed with PBS and the fluorescence staining was imaged using a confocal fluorescence microscope (Zeiss LSM 710, Germany).

2.11. Electrical stimulation setup design and manufacturing

Custom cell-culture plates were designed in SolidWorks (Dassault Systèmes SE, France). The wells were engineered to be connected in series to guarantee that the same electrical current magnitude passes through each cell culture well upon stimulation. The design (online available at figshare – https://figshare.com/s/3b1bf70b5201f236e5ea) was 3D printed in a Flashforge Inventor FDM 3D printer (Flashforge 3D printer, Jinhua, Zhejiang, China) using a C8 composite material filament (3D4Makers, Haarlem, The Netherlands).[44] The C8 material was printed according to manufacturer's specifications with an infill of 100%. Medical grade stainless steel wires 316LVM (1 mm in diameter) (Tegra Medical, Franklin, MA, USA) were used as electrodes (Fig. S7, ESI†). All the internal surfaces of the wells, except for the electrodes, were glued and isolated with PDMS (10 : 1, by weight ratio of base to curing agent) and left to dry overnight at 55 °C.

2.12. Osteogenic differentiation of hBM-MSCs on PCL-PEDOT and PCL scaffolds under ES

Prior to osteogenic induction, hBM-MSCs were seeded onto PCL-PEDOT (DVS(NaOH)-Gel) and PCL(NaOH) scaffolds at a density of 200 000 cells per scaffold and cultured for 5 days under standard expansion conditions at 37 °C and 5% CO_2 to allow the initial growth and migration of cells throughout the whole scaffold structure. Afterwards, the medium was replaced by osteogenic induction medium composed of DMEM supplemented with 10% FBS (MSC qualified), 10 mM of β-glycerolphosphate, 10 nM of dexamethasone, 50 μg mL^{-1} of ascorbic acid and 1% Anti–Anti and the cultured cell-seeded scaffolds were kept for additional 21 days with complete medium renewal every 2–3 days. For the electrical stimulation, the cell-seeded scaffolds were carefully transferred using sterile tweezers to the culture-plate device described in Section 2.11 and fresh osteogenic medium was added to the wells to completely immerse the scaffolds and electrodes. Electrical stimulation (AC, 1.2 V, period $T = 2$ s, 1 h day^{-1}) was applied daily during a 21-day culture period using an AFG1022 arbitrary function generator (Tektronix, Oregon, USA) based on previous studies. Non-stimulated PCL-PEDOT (DVS(NaOH)-Gel) and PCL(NaOH) scaffolds were used as controls. Cellular metabolic activity was assessed at days 1, 7, 14 and 21 using the AlamarBlue assay as described in Section 2.10. For each experimental group, six independent scaffolds were considered in the analysis ($n = 6$).

2.13. Assessment of MSC osteogenic differentiation and mineralization

2.13.1. Immunofluorescence analysis and xylenol orange staining. After 21 days of osteogenic differentiation with and without electrical stimulation, the samples were first washed with PBS and fixed in PFA 4% for 10 min. For the immunofluorescence analysis of bone specific proteins osteopontin (OPN) and type I collagen (COL I), cells were washed with PBS twice and permeabilized with blocking solution for 30 min at RT. After this, each sample was incubated overnight at 4 °C with anti-COL I or anti-OPN, both diluted 1 : 200 in staining solution (5% goat serum and 0.1% Triton-X-100 in PBS). Afterwards, samples were incubated with the secondary antibody goat anti-mouse AlexaFluor 488 (1 : 250 in staining solution) for 1.5 h at room temperature in the dark. Finally, samples were washed twice with PBS and counterstained with DAPI (1.5 μg mL^{-1} in PBS) for 5 min at 37 °C. Samples were visualized using confocal fluorescence microscopy (Zeiss LSM 710, Germany).

Xylenol orange staining was used to assess the presence of mineral deposits within the samples after 21 days of osteogenic differentiation with and without electrical stimulation. Briefly, previously fixed cell-seeded 3D scaffolds were incubated with xylenol orange red solution (20 mM) for 1 h at room temperature. The scaffolds were washed with PBS, counterstained with DAPI (1.5 μg mL^{-1} in PBS) for 5 min and washed once again with PBS. The fluorescence staining was imaged using a confocal fluorescence microscope (Zeiss LSM 710, Germany).

2.13.2. SEM. Fixed cells were dehydrated by incubation (30 min per step) with increasingly concentrated ethanol solutions (20%, 40%, 60%, 80%, and 96%). Cell drying was performed by incubating (30 min per step) the dehydrated cells with increasing amounts of HMDS added to 96% ethanol (1 : 2, 1 : 1, and 2 : 1). Finally, cells were left in pure HMDS and left to dry at RT in a fume hood. Cells were then coated with gold/palladium and imaged using SEM (Section 2.4.1.).

2.13.3. Alkaline phosphatase (ALP) quantification assay. ALP activity was assessed for hBM-MSCs after 21 days of osteogenic differentiation on PCL-PEDOT (DVS(NaOH)-Gel) and PCL(NaOH) scaffolds, without and with ES ($n = 3$). ALP activity was quantified using a colorimetric ALP kit (BioAssays Systems), following the manufacturer's guidelines. Briefly, samples were washed with PBS and incubated in a 0.2% Triton X-100 solution overnight at room temperature. *p*-Nitrophenyl solution (10 mM) was added to the lysates, and the obtained absorbance was measured at 405 nm using a microplate reader (Infinite 200 Pro; Tecan). The values were collected in duplicates for each sample, averaged and normalized to cell metabolic activity of the respective scaffold sample obtained using AlamarBlue™ assay.

2.13.4. Calcium staining and quantification. PCL(NaOH) and DVS(NaOH)-Gel samples, obtained after 21 days of hBM-MSC osteogenic differentiation, were washed with PBS and incubated in a 1 M HCl solution overnight under agitation at 150 rpm. The obtained supernatants were collected, and the calcium content was quantified using a colorimetric assay kit following the manufacturer's instructions. Briefly, 50 μL of sample and calcium standards were mixed with 90 μL of chromogenic reagent and 60 μL of calcium assay buffer. The absorbance was measured at 575 nm (n = 3), with acellular scaffolds used as blank controls. Calcium standard solutions (0, 0.4, 0.8, 1.2, 1.6 and 2.0 μg well^{-1}) were used to create a calibration curve, which allows the estimation of the calcium content in each sample. The obtained calcium content values were normalized to scaffold mass (mineralization assay) or the cell metabolic activity of each respective scaffold (MSC differentiation).

2.13.5. RNA extraction and gene expression analysis by quantitative real time polymerase chain reaction (qRT-PCR). Total RNA was extracted using the RNeasy Mini Kit following the manufacturer guidelines. The scaffolds were first incubated in lysis buffer under 200 rpm agitation for 1.5 h in ice before extraction and purification. RNA concentration was determined using a NanoVue Plus spectrophotometer (GE Healthcare, Chicago, IL, USA). cDNA was synthesized using a T100™ thermal cycler (BioRad, Hercules, CA USA). qRT-PCR analysis (n = 3) was performed using a StepOnePlus real-time PCR system (Applied Biosystems). The primer sequences used in the qRT-PCR analysis are presented in Table 2. The results obtained were analyzed using the $2^{-\Delta\Delta Ct}$ method to determine relative changes in specific osteogenic marker gene expression compared with the control sample (hBM-MSCs at day 0). Gene expression was primarily normalized to the housekeeping gene (*Gapdh*) and then determined as a fold-change relative to the baseline expression of the target genes in the control sample.

2.14. Statistical analysis

All data are presented as mean values ± standard deviations (std). Statistical analysis for the physico-chemical characterization data was performed using Microsoft Excel. Significant differences between groups were measured using the ANOVA test, followed by *post hoc* analysis and Bonferroni correction. $p < 0.05$ was considered statistically significant. For calcium quantification, ALP activity and qPCR analysis, statistical analysis of the data was performed using one-way ANOVA, followed by Tukey's *post hoc* test. GraphPad Prism version 7 software was used in the analysis and data were considered to be significant when p-values obtained were less than 0.05 (95% confidence intervals) ($^{*}p < 0.05$, $^{**}p < 0.01$, and $^{***}p < 0.001$).

3. Results and discussion

PCL and PEDOT:PSS are not compatible polymers due to their distinct physico-chemical properties and required processing strategies. PEDOT:PSS and PCL cannot be easily dispersed in a common solvent, which limits the production of reliable blend filaments for 3D-extrusion. Another limitation is that the stability and electroconductivity of PEDOT:PSS are temperature-dependent,[45] which limits its use in 3D-extrusion. Contrary to other materials, such as graphene, if PEDOT:PSS was to be physically dispersed in PCL its electroconductivity would be compromised. This would be due to the absence of pseudo-doping agents (*e.g.* DMSO, EG, and methanol)[46] and cross-linkers (*e.g.* GOPS, DVS, and oxetanes),[35,40,47] which hampers its electroconductivity and stability in water. Nevertheless, we were successful in optimizing a simple, reliable, and versatile method to produce electroconductive scaffolds using 3D-extruded PCL and PEDOT:PSS coatings. This was done through harnessing the material chemistry of both PCL, through alkaline treatment, and PEDOT:PSS, through optimization of the cross-linkers used (GOPS and DVS), to create both electroconductive and stable bi-layer composites. Finally, since no direct synthesis was performed for the coating, as explored in other works in the literature,[48,49] the number of side-products and residues in the final scaffolds is also lower.

3.1. Coating performance and stability on extruded films

The goal of this work was to produce an electroconductive and stable 3D-extruded scaffold suitable for bone tissue engineering applications. Our approach relied on coating a 3D-printed PCL scaffold with PEDOT:PSS using two different cross-linkers: GOPS and DVS. These cross-linkers have been widely studied for the production of water-stable PEDOT:PSS substrates for diverse electronic applications.[40,50,51] Due to their cross-linking chemistry, we envisaged these to be capable of both stabilizing PEDOT:PSS and anchoring it to the PCL surface following a preliminary alkaline treatment of PCL. This treatment of PCL with NaOH(aq) is expected to promote some superficial PCL hydrolysis, forming carboxylic/hydroxyl groups that could react with the cross-linking agent. The treatment should improve the wettability of the PCL surface. The use of GOPS and DVS

Table 2 Sequences for the primers used in this study

Gene	Fwd primer sequence	Rev primer sequence
GAPDH	5′-GGTCACCAGGGCTGCTTTTA-3′	5′-CCTGGAAGATGGTGATGGGA -3′
RUNX2	5′-AGATGATGACACTGCCACCTCTG-3′	5′-GGGATGAAATGCTTGGGAACT-3′
OSX	5′-CTGGACATGACACACCCCTAT-3′	5′-GCTGGATTAAGGGGAGCAAAG-3′
COL I	5′-CATCTCCCCTTCGTTTTTGA-3′	5′-CCAAATCCGATGTTTCTGCT-3′
OC	5′-TGTGAGCTCAATCCGGCATGT-3′	5′-CCGATAGGCCTCCTGAAGC-3′
OPN	5′-CAGGTCTGCGAAACTTCTTAG-3′	5′-CTCCATTGACTCGAACGACTC-3′
CACNA1C	5′-GTACAAAGACGGGGAGGTTGAC-3′	5′-GTAGTTGTAGATGGGGCCCTTG-3′

cross-linkers was necessary to produce a homogeneous electroconductive coating of PEDOT:PSS. This was due to the inability of commercial PEDOT:PSS solution to form a continuous film on either PCL and PCL(NaOH). Finally, gelatin was included in the PEDOT:PSS formulation to increase the bioactivity of the coating obtained. We analyzed the integrity of the PEDOT:PSS coating on extruded PCL films by evaluating their contact angle, electroconductivity and stability in PBS for 21 days.

3.1.1. Surface properties. The first step was to analyze the surface properties of PCL and PEDOT:PSS coated PCL extruded films through contact angle measurement and FTIR analysis. Films were used instead of the scaffold in order to minimize the influence of substrate topography and porosity on the obtained results.[52,53] The results are summarized in Fig. 3(A),(B) and Table 3. PCL and PCL(NaOH) samples, our controls, yielded contact angles of 80° and 59°, indicating that alkaline treatment was successful in increasing the hydrophilicity of the surface in a statistically significant way. When solution 1 (PEDOT:PSS + GOPS) was used for coating, the contact angle decreased to 57° for the pristine scaffold (GOPS) but remained constant at 56° for the alkaline-treated scaffold (GOPS(NaOH)). When gelatin was added to the coating of PCL-NaOH scaffolds (solution 2), the contact angle further decreased to 18° (GOPS(NaOH)-Gel), which was statistically different from sample GOPS(NaOH).

When solution 3 (PEDOT:PSS + DVS) was used for coating, both PCL and PCL(NaOH) samples, the contact angle decreased to 49° (DVS) and 46° (DVS(NaOH)), respectively. When gelatin was added to the coating of PCL-NaOH scaffolds (solution 4), the contact angle greatly decreased to 7.9° (DVS(NaOH)-Gel). Such a decrease was statistically significant for the sample DVS(NaOH).

The FTIR spectra for all samples are depicted in Fig. 3(B) (and also Fig. S1 (raw materials), ESI†). The spectra of PCL (spectrum a) and PCL(NaOH) (spectrum b) evidence the characteristic peaks at 2938/2861 cm^{-1}, for asymmetric/symmetric CH_2 bands, 1704 cm^{-1}, for carbonyl groups, and 800–1500 cm^{-1}, for the characteristic fingerprint region.[54,55] The same peaks are visible for samples GOPS (spectrum c), GOPS(NaOH) (spectrum d), DVS (spectrum f) and DVS(NaOH) (spectrum g), along with small peaks at 1538 cm^{-1}, for aromatic rings of PEDOT:PSS.[56] The peak centered at 3480 cm^{-1}, for free OH/NH groups is also visible but it is more intense for samples GOPS(NaOH)-Gel (spectrum e) and DVS(NaOH)-Gel (spectrum h). The spectrum of DVS(NaOH)-Gel (spectrum h in Fig. 3(B)) and to a lesser extent the spectrum of GOPS(NaOH)-Gel show the PCL characteristic peaks in the 800–1500 cm^{-1} spectral region, but their relative intensity is much lower, suggesting the presence of a thicker coating layer. Finally, the addition of gelatin to the PEDOT:PSS coating (spectra e and h) is associated with a change in the fingerprint region. This is more evident for sample DVS(NaOH)-Gel, whose respective peaks change in intensity and shape when compared with those of DVS(NaOH)-Gel. Such a change is similar to that observed by Sridharan and colleagues[57] for coaxial PCL/Gelatin fibers and indicates the formation of a 2 layer composite consisting of PCL and a gelatin-coating.

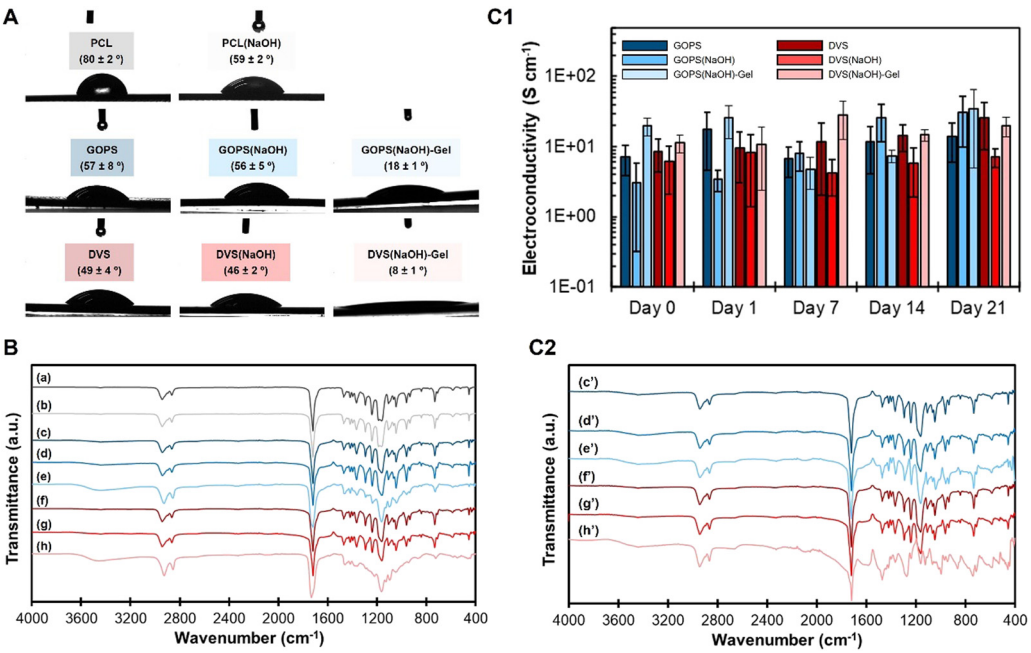

Fig. 3 Characterization of the different PEDOT-based coatings tested on 3D-extruded PCL films (A) Contact angle profiles obtained for the different combinations tested (mean ± std, n = 6, * means $p < 0.05$ compared to PCL). (B) Respective FTIR spectra of the samples: (a) PCL, (b) PCL(NaOH), (c) GOPS, (d) GOPS(NaOH), (e) GOPS(NaOH)-Gel, (f) DVS, (g) DVS(NaOH), and (h) DVS(NaOH)-Gel. (C) Stability assay results for 21 days for the different PEDOT-based coatings tested; (C1) electroconductivity changes (n = 5) at different timepoints and (C2) FTIR spectra recorded at day 21 of samples (c′) GOPS, (d′) GOPS(NaOH), (e′) GOPS(NaOH)-Gel, (f′) DVS, (g′) DVS(NaOH), and (h′) DVS(NaOH)-Gel.

Table 3 Summary of the physico-chemical properties of the different PEDOT:PSS coatings tested in this work (results presented as mean ± std, (*) means $p < 0.05$ when compared to PCL, (+) means $p < 0.05$ when compared with PCL(NaOH), (a) means $p < 0.05$ when compared to GOPS/DVS samples without gelatin)

Films	PCL	PCL(NaOH)	GOPS	GOPS(NaOH)	GOPS(NaOH)-gel.	DVS	DVS(NaOH)	DVS(NaOH)-gel.
Electroconductivity (S cm^{-1})	—	—	7.2 ± 3.2	3.0 ± 2.7	20.1 ± 5.7	8.6 ± 4.2	6.1 ± 4.0	11.3 ± 3.2
Contact angle (°)	79.9 ± 2.0	59.0 ± 2.3 (*)	57.2 ± 8.0 (*)	55.8 ± 4.9 (*)	18.3 ± 0.9 (*)(a)	49.0 ± 4.1 (*)	46.4 ± 2.1 (*)	7.9 ± 0.7 (*)(a)

Scaffolds	PCL	PCL(NaOH)	GOPS	GOPS(NaOH)	GOPS(NaOH)-gel	DVS	DVS(NaOH)	DVS(NaOH)-gel
Young's modulus (MPa)	8.8 ± 0.2	8.6 ± 0.3	8.8 ± 0.5	8.4 ± 0.5	10.2 ± 0.1(*)(+)	8.8 ± 0.2	9.1 ± 0.1	10.6 ± 0.0(*)(+)
Mineralization at day 21 (ng mg^{-1})	0.41 ± 0.36	0.45 ± 0.24	—	2.66 ± 0.32 (*)(+)	3.08 ± 0.21(*)(+)	—	1.29 ± 0.57	1.97 ± 0.63
Adhesion (%)	10.1 ± 1.4	12.3 ± 1.3	—	21.0 ± 5.5	14.2 ± 2.2	—	9.8 ± 2.3	21.7 ± 5.9

DVS-based samples had the most hydrophilic coatings. This is in line with our previous observations for PEDOT:PSS films spin-coated on glass substrates.[40] Samples whose PEDOT:PSS coating contained gelatin presented the lowest contact angle values of our study. In a different work, Ghasemi-Mabarakeh and colleagues[58] observed that increasing the gelatin content of PCL-gelatin electrospun fibers leads to decreased contact angles. In our work, gelatin is present within the PEDOT:PSS layer. As such, these results, together with the FTIR spectra, indicate a successful incorporation of gelatin in the coating of our samples, which can potentially improve their bioactivity and promote the adhesion and growth of MSCs.[59,60]

3.1.2. Electroconductivity and chemical stability. The electroconductivity of the different PEDOT:PSS coatings produced was evaluated on 2D films, and not on 3D scaffolds, to facilitate the necessary measurements. The results are summarized in Fig. 3(C1) and Table 3. Both GOPS (7.2 S cm^{-1}) and DVS (8.6 S cm^{-1}) samples had similar electroconductivity values, indicating the formation of an electroconductive coating at the surface of pristine PCL films. Samples GOPS(NaOH) (3.0 S cm^{-1}) and DVS(NaOH) (6.1 S cm^{-1}) were also electroconductive, indicating that the alkaline treatment of PCL films does not interfere with the formation of the coating. The obtained electroconductivity values are higher than physiological values reported for cancellous/trabecular bone (0.079 S m^{-1}).[61] Considering our final application of ES of cultured cells, we believe that such a difference might not negatively impact cell health and/or differentiation.

Electroconductivity slightly increased for samples GOPS (NaOH)-Gel (20.1 S cm^{-1}) and DVS(NaOH)-Gel (11.3 S cm^{-1}), suggesting a positive effect of gelatin incorporation on electroconductivity. Such a phenomenon was not expected, as gelatin is an insulator. According to Huang and colleagues,[62] low-molecular weight poly(ethylene oxide) has pseudo-doping properties and is capable of cross-linking PSS through its ether groups in an acidic environment. We speculate that a similar phenomenon could have happened between gelatin and PEDOT:PSS, which can also explain the electrical stability of previously reported gelatin-PEDOT:PSS scaffolds.[63] To better clarify this phenomenon, we studied the corresponding spin-coated PEDOT:PSS films.

The main results for the obtained spin-coated PEDOT:PSS films are summarized in Fig. S3 (ESI†). Sample fDVS is the most electroconductive (1071 S cm^{-1}) among the tested samples (Fig. S3(A), ESI†). It is statistically different from samples fDVS-Gel (290 S cm^{-1}), fGOPS (240 S cm^{-1}) and fGOPS-Gel (67 S cm^{-1}). Such a trend was not observed for the PCL-PEDOT:PSS films. A closer analysis of the thickness of the spin-coated films (Fig. S3(B), ESI†) reveals dramatic differences. Samples fGOPS-Gel (46 305 Å) and fDVS-Gel (14 917 Å) showed higher thicknesses when compared with samples fGOPS (1333 Å) and fDVS (869 Å). These results suggest that the amount of immobilized material is higher for samples fGOPS-Gel and fDVS-Gel. Finally, we used the UV/Vis (Fig. S3(C), ESI†) and NIR (Fig. S3(D), ESI†) spectra of the obtained spin-coated PEDOT:PSS samples to evaluate how gelatin interferes with PEDOT:PSS. The addition of gelatin does not significantly affect the characteristic peak at 223 nm, but instead induces the formation of a smaller peak at 260 nm. Addition of gelatin negatively interferes with the conduction band, especially in sample fGOPS-Gel (1100–2300 nm) when compared to fGOPS. This effect is less pronounced in sample fDVS-Gel (1400–2300 nm), where the conduction band is slightly less intense than in fDVS. As such, we conclude that the addition of Gel to PEDOT:PSS films negatively interferes structurally with PEDOT:PSS, which affects its electroconductivity, but the use of DVS as the cross-linker avoids this.

The stability of the different PEDOT:PSS coatings was evaluated *in vitro* and by mimicking the physiological conditions of pH and osmolarity. The results obtained are shown in Fig. 3(C1) (electroconductivity changes for 21 days), Fig. 3(C2) (FTIR of samples at day 21), and Fig. S2 (ESI†) (FTIR of samples at days 1, 7 and 14). Electroconductivity of the coating was stable for all samples through the whole duration of the assay, with no significant statistical differences found among the samples from different timepoints.

FTIR shows minimal differences regarding the chemistry of all samples. The exception was sample DVS(NaOH)-Gel, which displays the most complex spectra of all samples. Its FTIR spectra at day 1 are completely different from those recorded for the dry film (Fig. 3(B)), in particular in the region 2000–800 cm^{-1}. Starting at day 1, and for the following 7 and 14 days (Fig. S2, spectra f, ESI†), a broad peak region appears between 1200 cm^{-1} and 1600 cm^{-1}, which matches the characteristic fingerprint region of gelatin containing amide peaks. A long band between 2000 cm^{-1} and 3600 cm^{-1} is visible, suggesting

the co-existence of free amine/hydroxyl and ketone groups at the superficial region of the sample.[64] While these can arise from the EG additive, as described by Mantione and colleagues,[51] other potential sources are the gelatin or cross-linked PEDOT:PSS.[40,65] At day 21 (Fig. 3(C2), spectrum h′) the long band at 2000–3600 cm^{-1} becomes less intense, and the fingerprint peaks of gelatin (800–1500 cm^{-1}) are still visible, and the fingerprint region of PCL (800–1500 cm^{-1}) is not observed, suggesting a potential swelling of the PEDOT:PSS coating.

The characteristic gelatin peaks at 1200–1650 cm^{-1} (Fig. S1, spectrum c, ESI†) are visible on the FTIR spectra of both samples GOPS(NaOH)-Gel and DVS(NaOH)-Gel at both days 0 and 21. These peaks are associated with amide groups,[66] which present reactive spots for GOPS/DVS nucleophilic attack and consequent amide-to-ester conversion during cross-linking.

The spectra of both samples GOPS(NaOH)-Gel and DVS(NaOH)-Gel change after 21 days of incubation with PBS. For sample GOPS(NaOH)-Gel, the fingerprint regions at days 21 (Fig. 3(C2), spectra e′, 800–1.400 cm^{-1}) 14, 7 and 1 (Fig. S2, spectra c, ESI†) resemble that of GOPS(NaOH) at day 0 (Fig. 3(B), spectra e). Since no changes in electroconductivity were found for this same sample, we hypothesize that these do not compromise the PEDOT:PSS coating *per se*. For sample DVS(NaOH)-Gel, the fingerprint region changes and new peaks at 1471 cm^{-1}, 1271 cm^{-1} and 995 cm^{-1} appear. These peaks partly overlap those of gelatin raw material (Fig. S1, spectrum c, ESI†). Similar changes are observed for the other timepoints of the stability assay (Fig. S2, ESI†). While the DVS(NaOH)-Gel system is chemically complex, making the changes in the fingerprint region difficult to interpret, we can speculate that these changes can be attributed to gelatin chain rearrangement that occurs after water retention. In this case, the obtained coating is more stable and more efficient at retaining chemically bonded gelatin, which prevents its lixiviation and allows the coating to retain its bioactivity. As such, we hypothesize that sample DVS(NaOH)-Gel will have a higher bioactivity when compared with sample GOPS(NaOH)-Gel.

3.2. Coating performance on extruded PCL scaffolds

The data obtained for the PEDOT:PSS-coated PCL films suggest the formation of an electroconductive, stable (up to 21 days) and thin coating in all samples tested. The next step of our work was to produce corresponding 3D PEDOT:PSS-coated PCL scaffolds that can be used for bone TE applications. We evaluated the effect of different PEDOT:PSS coatings on critical properties of the obtained scaffolds, including morphology, mechanical properties, *in vitro* mineralization, MSC adhesion and proliferation, and electrical field distribution.

3.2.1. Morphology and mechanical properties. 3D-extruded PCL scaffolds were treated and/or coated with the different PEDOT:PSS solutions already tested. The design was adapted from our previous work: the orthogonal structure (0–90° between fibers in two consecutive double-printed layers).[67] A similar design of the scaffold used in this work, including fiber/pore diameter and porosity, was used in our previous work for BTE applications.[26] In that work, we improved scaffold bioactivity for bone applications by immobilizing the decellularized MSC-derived ECM on its surface. Other works also made use of similar scaffold design for creating electroconductive and/or bioactive scaffolds for bone regeneration strategies.[24,32,68,69] Nevertheless, changing the scaffold design to a more bone biomimetic structure can be easily achieved by CAD design methods or through the digitalization of a reconstructed micro-CT image of bone trabeculae tissue.

The morphology of the obtained PCL and PCL-PEDOT:PSS coated scaffolds (SEM and MicroCT) is shown in Fig. 4. SEM images reveal an overall smooth surface in all the obtained samples. Small cavities can be seen in the higher magnification images of samples PCL, GOPS(NaOH), GOPS(NaOH)-Gel, DVS(NaOH) and DVS(NaOH)-Gel, which originate from PCL.[24] They can provide extra surface area for cell adhesion. Other

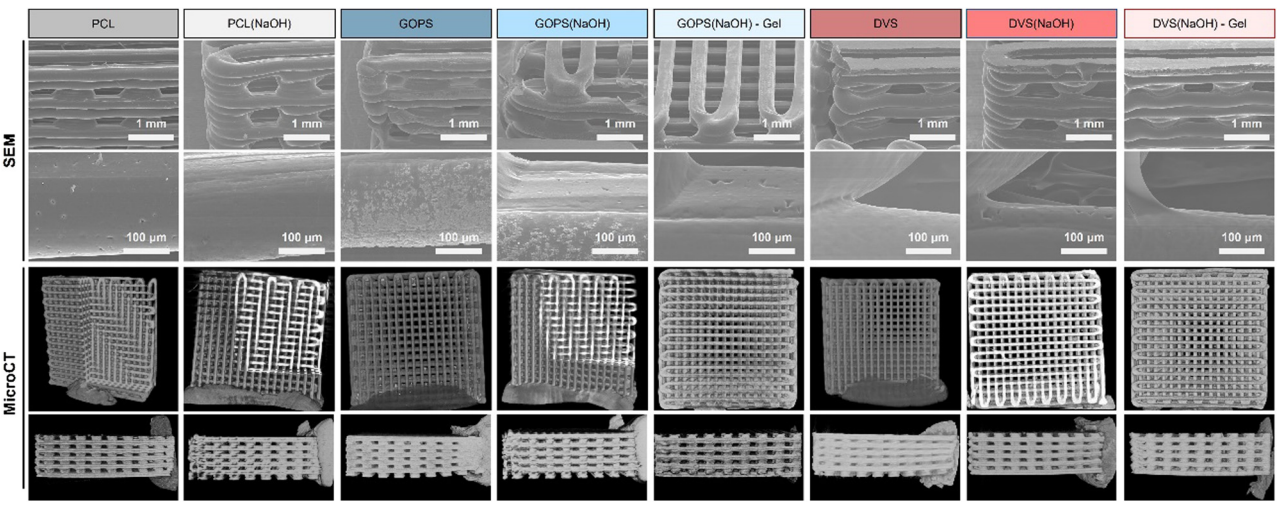

Fig. 4 SEM images of the PCL and PCL-PEDOT:PSS-based scaffolds produced with different combinations of cross-linker (GOPS or DVS) and bioactive motifs (Gel). Scale bars are depicted in the SEM images.

imperfections are seen, such as powder deposits (GOPS, GOPS(NaOH)) and a flat first layer (DVS, DVS(NaOH) and DVS(NaOH)-Gel), but they are attributed to the sample preparation process for SEM analysis.

MicroCT images also evidence homogeneous scaffolds with limited imperfections, independently of the chemical treatments and coating solutions used. The different structural properties of the scaffolds are summarized in Table 4. All scaffolds have a pore interconnectivity of around 100%, which is highly favorable for the diffusion of nutrients, oxygen and soluble factors, as well as cell migration and proliferation. Other structural parameters are relatively constant and do not vary for different samples, including porosity (59%), superficial area per volume (14.4 mm^{-1}), pore size (293 μm) and fiber diameter (305 μm). This indicates that the scaffold fabrication process is highly reproducible and that both the alkaline treatment and PEDOT:PSS coating of the scaffolds do not greatly affect the scaffolds' morphological features.

In this work, the average porosity of the scaffolds obtained is 59%, slightly lower than the average porosity found for trabecular bone as described by Renders and colleagues[70] (79.3 ± 5.1%) but higher than the value described for cortical bone porosity by Bousson and colleagues[71] (15.88 ± 9.87%). We consider that the value obtained is appropriate for future bone TE applications, as it allows the growth and osteogenic differentiation of MSCs, with free flow of culture media.[26] Potentially, these scaffolds can be used for the regeneration of trabecular bone or be integrated into cortical bone after appropriate cell colonization and ECM deposition.[72]

The next step in our work was to evaluate the mechanical properties of the obtained scaffolds under compression, to mimic the loads naturally exerted in bone tissue *in vivo*. The main results, including the obtained stress–strain curves, the compressive Young's modulus, and the maximum stress, are summarized in Fig. 5 and Table 3. The compressive modulus of PCL (8.8 ± 0.2 MPa) and PCL(NaOH) (8.6 ± 0.3 MPa) scaffolds indicates that the chemical treatment with NaOH did not impair the stiffness of the scaffold. Compared with PCL and PCL(NaOH) samples, no statistically significant changes in the compressive modulus occurred for samples GOPS (8.8 ± 0.5 MPa), GOPS(NaOH) (8.4 ± 0.5 MPa), DVS (8.8 ± 0.2 MPa), and DVS(NaOH) (9.1 ± 0.1 MPa). This indicates that the presence of a PEDOT:PSS coating does not compromise the stiffness of the scaffold. The incorporation of gelatin leads to a statistically significant increase in the compressive moduli of samples GOPS(NaOH)-Gel (10.2 ± 0.1 MPa) and DVS(NaOH)-Gel (10.6 ± 0.0 MPa). The obtained compressive modulus is lower than that obtained in our previous works,[22] which we attribute to the use of a different commercially available PCL filament. Huang and colleagues[73] tested PCL scaffolds prepared with different bioinks and found that the use of organic solvents for preparation (*e.g.*, 2-butoxyethanol) lead to a decrease in the final scaffold stiffness (10 MPa). The authors attribute this decrease to the residual solvent that increases the PCL chain mobility and reduces the crystallization of PCL. However, osteogenic differentiation efficiency was not compromised in these scaffolds.

The Young's modulus values obtained for all scaffolds under compressive testing showed an inferior stiffness when comparing to the range found for cancellous/trabecular bone (50–100 MPa).[17] However, these values vary greatly depending on the bone origin along with the sex (male/female vertebrae – 55.6/35.1 MPa; male/female tibia – 34.6/23.1 MPa), age and health conditions of the sample donor.[74] The lower value obtained for the compressive modulus should not be seen as a limitation for using these scaffolds in bone applications, since bone TE strategies for defect repair in most demanding regions may include central rigid supports to guarantee proper load transfer and surroundings until cell colonization and mineralization can improve their mechanical properties.[75–77] The obtained Young's modulus for the obtained PCL scaffolds is lower than the values reported in previous works using similar scaffolds.[22,33,78] However, a study from Olubamiji and colleagues[79] reported compressive modulus within the same range of the ones obtained in this work for PCL scaffolds with the same fiber orientation (0–90°), fiber diameter and similar porosity. These differences can be due to the properties of the used PCL raw material, including molecular weight and crystallinity.[79,80] It was previously shown that the mechanical properties could be further finetuned by changing the architecture of the designed PCL scaffolds.[21,79] This shows the versatility of our developed PCL-PEDOT:PSS scaffolds and its potential applications in BTE.

The maximum stress of samples GOPS (1.5 ± 0.4 MPa), GOPS(NaOH) (1.2 ± 0.4 MPa), DVS (1.3 ± 0.2 MPa), and DVS(NaOH) (1.6 ± 0.2 MPa) decreased significantly when compared with those of PCL and PCL(NaOH) samples, which did not break at 50 N/5 MPa. This suggests that the incorporation of the PEDOT:PSS coating on PCL scaffolds increases the fragility of the scaffolds. The incorporation of gelatin in the PEDOT:PSS coating improved the maximum stress of samples GOPS(NaOH)-Gel (no break) and DVS(NaOH)-Gel

Table 4 Summary of the different structural properties of the scaffolds (results are presented as the obtained value when n = 1, or as mean ± std when n = 3)

Scaffolds	PCL	PCL(NaOH)	GOPS	GOPS(NaOH)	GOPS(NaOH)-Gel	DVS	DVS(NaOH)	DVS(NaOH)-Gel
Interconnectivity (%)	99.9	100.0	99.9	100.0	99.9	99.9	100.0	99.9
Porosity (%)	59.1	61.1	59.8	59.9	58.9	57.1	59.5	59.8
Superficial area per volume (mm^{-1})	14.3	15.2	14.3	14.4	14.8	13.3	13.49	15.3
Pore size (μm)	285 ± 33	287 ± 46	308 ± 42	294 ± 27	294 ± 28	280 ± 47	297 ± 35	299 ± 30
Fiber diameter (μm)	311 ± 30	311 ± 50	290 ± 47	311 ± 27	308 ± 37	315 ± 50	304 ± 32	292 ± 30

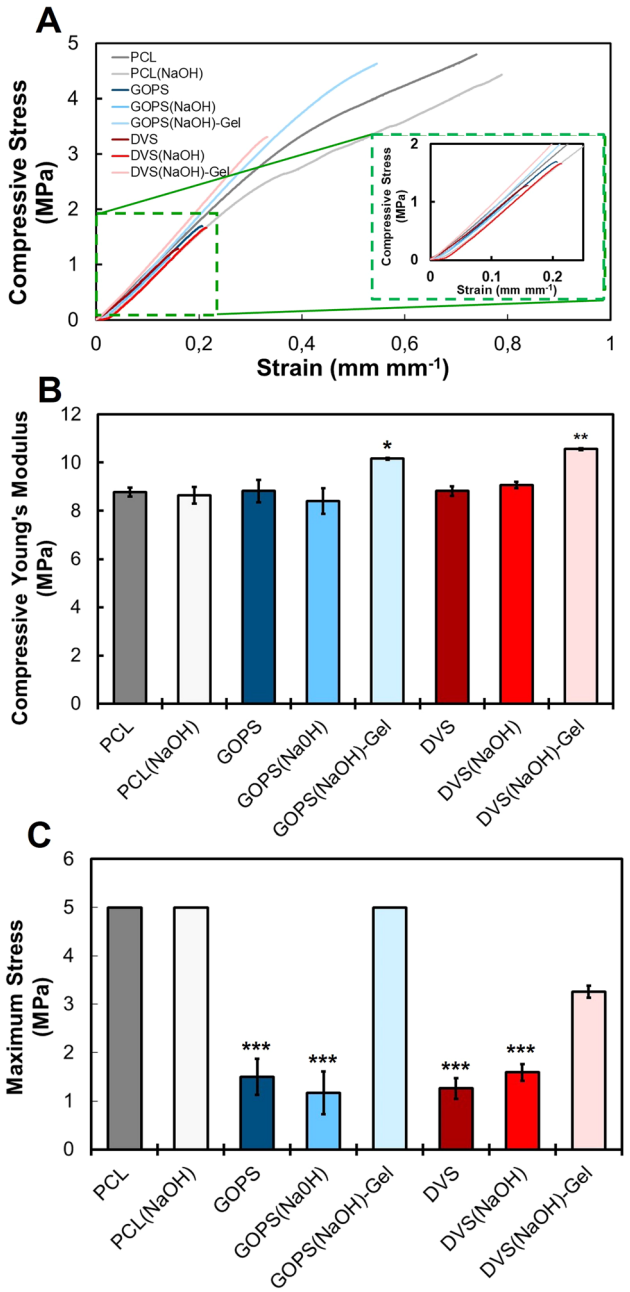

Fig. 5 Mechanical performance of PCL-PEDOT scaffolds and respective PCL controls under compressive testing: (A) stress–strain curves, (B) compressive Young's modulus and (C) maximum stress (mean ± std, n = 5; (*) means $p < 0.05$ compared to all samples except GOPS; (**) means $p < 0.05$ compared to all samples; (***) means $p < 0.05$ when compared to DVS(NaOH)-Gel).

(3.3 ± 0.1 MPa). This is potentially due to the effect of more favorable mechanical properties of gelatin on the PEDOT:PSS coating.[63]

We hypothesized that the changes in the mechanical properties of PCL-PEDOT:PSS scaffolds could be due to changes in the materials chemistry due to pH and heat treatment. To understand this, we treated pristine PCL and PCL(NaOH) scaffolds with an aqueous solution of H_2SO_4 with a pH of 2, to mimic PEDOT:PSS incubation, and/or heated them at 50 °C, to mimic the drying/cross-linking conditions. The obtained results are summarized in Fig. S3 (ESI†). Neither of the conditions tested impaired the stress–strain curves of both PCL and PCL(NaOH) scaffolds, as neither of the scaffolds broke before 50 N/5 MPa was reached. What is also remarkable is the statistically significant increase in the compressive modulus of the samples. This leads us to hypothesize that the changes in the mechanical properties of PCL-PEDOT:PSS scaffolds are mainly caused by the PEDOT:PSS layer. It is possible that such a drastic change in the maximum stress of the samples is a consequence of the cross-linking between PCL and the PEDOT:PSS layer. Due to the brittleness of PEDOT:PSS, the PEDOT:PSS layer should break first during the compressive test.[81,82] The presence of cross-linking bonds between PEDOT:PSS and PCL, *via* GOPS or DVS, can lead to the propagation of cracks to the PCL scaffold, favoring its mechanical break.

3.2.2. Bioactivity and *in vitro* performance. The developed PCL-PEDOT:PSS scaffolds present interesting physico-chemical and mechanical properties to be used for ES studies to improve the osteogenic differentiating MSCs. Before we conducted those experiments, we decided to evaluate the bioactivity and *in vitro* performance of the obtained scaffolds. First, we conducted a mineralization assay using SBF, followed by a proliferation assay with MSCs.

The suitability of scaffolds for bone TE applications will depend on their ability to be (bio)mineralized. In mature bone, hydroxyapatite [$(Ca)_{10}(PO_4)_6(OH)_2$] (HAp) composes 60% of the tissue *vs.* 40% of organic components, providing both mechanical and structural support to the body and acting as a calcium and phosphate ion deposit for the cells. Osteoblasts can regulate HAp formation through regulation of calcium secretion and phosphate metabolism. HAp is immobilized by type 1 collagen fibrils, the most abundant organic compound in bone (90%).[83,84]

The ability of a material to allow the deposition of HAp can greatly contribute to bone regeneration and allow adequate osteoblast/osteoclast colonization.[42] We investigated the biomineralization of our scaffolds using SBF, a synthetic solution with the ionic composition and concentration as the human plasma. SBF has been used to evaluate the biomineralization of materials suitable for bone repair applications without the need for living cells. When materials are dipped in SBF, HAp gradually deposits on their surface. The more HAp is deposited, the more efficient cell colonization and tissue integration are expected to be. Fig. 6 summarizes the main results obtained. HAp deposition was evaluated through quantification of calcium content in the scaffolds tested (Fig. 6(A)) and complemented with SEM visualization of the deposited mineral crystals (Fig. 6(B)). Both PCL and PCL(NaOH) samples have small crystals deposited at their surface, and these were visually more numerous in PCL(NaOH). Both scaffolds had similar amounts of calcium (0.41 ± 0.36 ng mg^{-1} *vs.* 0.44 ± 0.24 ng mg^{-1} respectively), and no statistically significant difference was found between them. The amount of calcium was higher for samples GOPS(NaOH) (2.66 ± 0.32 ng mg^{-1}),

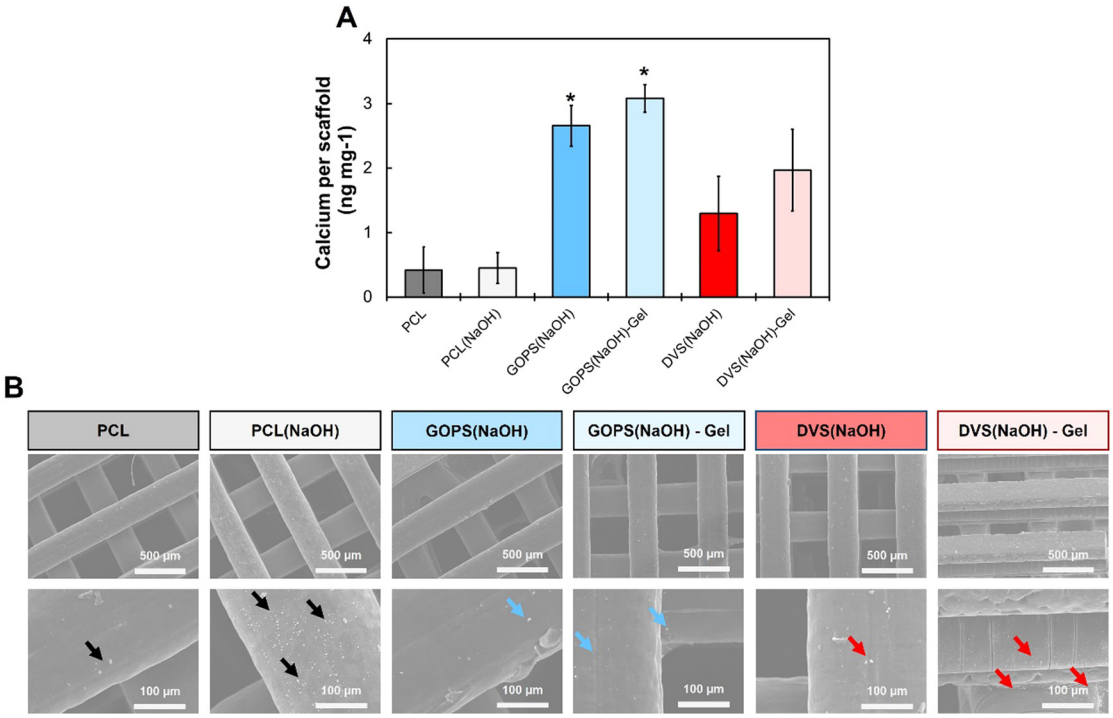

Fig. 6 Mineralization assay using SBF (A) Quantification of calcium content per different treatments tested (mean ± std, (*) means $p < 0.05$ when compared to PCL and PCL(NaOH)); (B) SEM images of the different scaffolds after 21 days of incubation in SBF (crystals locations highlighted with arrows). Scale bars are depicted in the images.

GOPS(NaOH)-Gel (3.08 ± 0.21 ng mg^{-1}), DVS(NaOH) (1.29 ± 0.58 ng mg^{-1}) and DVS(NaOH)-Gel (1.97 ± 0.63 ng mg^{-1}). Calcium content values for samples GOPS(NaOH) and GOPS(NaOH)-Gel were the highest among the different conditions and both were statistically different from those of pristine PCL and PCL(NaOH). Calcium contents for samples DVS(NaOH) and DVS(NaOH)-Gel were slightly lower and not statistically different from those for PCL/PCL(NaOH) samples and GOPS(NaOH)/GOPS(NaOH)-Gel samples. SEM images (Fig. 6(B)) revealed the presence of small crystal deposits on all samples, confirming the presence of HAp deposited on all the PEDOT:PSS coated samples.

The *in vitro* mineralization of PCL scaffolds had been described before. Xie and colleagues[75] report the mineralization of PCL and PCL-poly(dopamine) electrospun fibers in 10x SBF (SBF ten times more concentrated). PCL alone allowed mineralization, with crystals being deposited at its surface, while PCL-poly(dopamine) greatly enhanced mineralization, with denser and regular crystals being deposited at its surface. The inclusion of electroconductive polymers and/or other bioactive cues also favors the mineralization of scaffolds. Park and colleagues[85] reported an enhancement in the mineralization of PCL fibers when increasing amounts of poly(thiophene) nanoparticles are incorporated. Rajzer and colleagues[86] reported successful mineralization of PCL electrospun fibers in 1x SBF when nano-HAp powder was incorporated, and even when poly(aniline) was printed on top. Overall, these observations support our observations of successful mineralization of both PCL/PCL(NaOH) samples and the enhancement observed when PEDOT:PSS coating was applied.

The differences in the calcium content between GOPS(NaOH) and DVS(NaOH) samples can be explained by differences in the surface properties of the PEDOT:PSS coatings obtained. Both GOPS and DVS react with PSS, *via* the formation of sulfonate esters (R–O–SO_2–R′), to create insoluble moieties that anchor PEDOT chains. PEDOT:PSS films cross-linked with GOPS, which already possesses silicate (Si–O–CH_3) groups, will also possess siloxane (Si–O–Si) groups at their surface.[50] Siloxane groups are also present on bioglass, a material that greatly promotes mineralization of scaffolds.[87] PEDOT:PSS films cross-linked with DVS are predicted to have sulfonyl (R–SO_2–R′) and ether (R–O–R′) groups, after cross-linking with both PSS and EG.[51,88] Calcium sulfate, a similar compound enriched in sulfur-based functional groups, has inferior *in vivo* performance for scaffold mineralization when compared with standard HAp.[89] We hypothesize that siloxane and silicate groups from GOPS are more effective in adsorbing calcium than the sulfonyl/ether groups from DVS, which explains the different calcium contents in samples GOPS(NaOH) and DVS(NaOH).

The addition of gelatin to the PEDOT:PSS coating further enhances the calcium content of the coatings. Gelatin is mainly composed of denatured type 1 collagen, the main component of the bone ECM. Collagen promotes tissue mineralization through a combined mechanism of calcium absorption, potentially promoted by charged aminoacids, and mineral entrapment between fibrils. While the 3D structure of collagen is lost

in gelatin, it is possible that the same charged aminoacids can serve as HAp nucleation sites and promote mineralization. This can explain the observed improvements in calcium content (Fig. 6(A)) and deposited minerals (Fig. 6(B)) observed for both samples GOPS(NaOH)-Gel and DVS(NaOH)-Gel.

Overall, the four combinations of PCL-PEDOT:PSS scaffolds tested allowed successful biomineralization. The results suggest (1) a positive influence of the PEDOT:PSS coating on HAp deposition, (2) a PEDOT:PSS coating cross-linked with GOPS promotes higher calcium deposition than the PEDOT:PSS coating cross-linked with DVS, and (3) the addition of gelatin slightly increases calcium deposition on the scaffolds.

The final step of our *in vitro* performance studies was to conduct a proliferation assay with MSCs. The main results are summarized in Fig. 7 and Table 3. The obtained metabolic activity is associated with the cell number, and changes in its value can be correlated with changes in cell number. The values obtained at day 1 were used to estimate cell adhesion (Table 3). The ANOVA test suggested statistically significant differences in adhesion between samples, but we could not find such differences after our *post hoc* analysis. The highest values of cell adhesion were observed for DVS(NaOH)-Gel (21.7 ± 5.9), GOPS(NaOH) (21.0 ± 5.5) and GOPS(NaOH)-Gel (14.2 ± 2.2). A constant increase in metabolic activity (Fig. 7(A)) was observed for all samples, except GOPS(NaOH)-Gel. At day 7, the cell metabolic activity was the highest for DVS(NaOH)-Gel, followed by PCL(NaOH), PCL and GOPS(NaOH). The obtained cells at day 7 were visualized using DAPI-Phalloidin staining. Both PCL and PCL(NaOH) (Fig. 7(B1) and (B2) respectively) allowed a homogeneous colonization of the scaffold by the MSCs. Samples GOPS(NaOH) and DVS(NaOH) (Fig. 7(C1) and (D1) respectively) show scaffold colonization by MSCs, but they form clumps instead and make less contact with the PEDOT:PSS coating. For samples GOPS(NaOH)-Gel and DVS(NaOH)-Gel (Fig. 7(C2) and (D2) respectively), cell spreading and colonization on the scaffolds is improved.

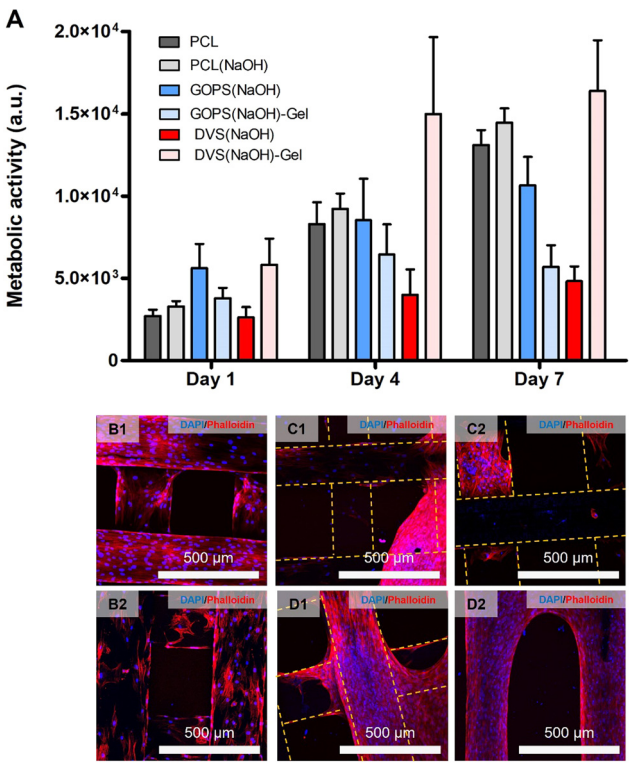

Fig. 7 (A) Metabolic activity of MSCs cultured for 7 days on different scaffolds (mean ± std, n = 4) and respective DAPI/Phalloidin staining at day 7 for the different scaffolds tested: (B1) PCL, (B2) PCL(NaOH), (C1) GOPS(NaOH), (C2) GOPS(NaOH)-Gel, (D1) DVS(NaOH) and (D2) DVS(NaOH)-Gel. Dashed lines represent the location of the filaments.

Our results suggest the incorporation of gelatin in samples cross-linked with DVS favored cell adhesion, proliferation, and scaffold colonization. This was expected since gelatin has been used in the design of scaffolds suitable for bone TE applications.[90–92] The obtained positive cell and mineralization assay outcomes justify our choice of continuing further ES studies with sample DVS(NaOH)-Gel.

3.2.3. Electrical field simulation using FEA. In a previous work, we showed that the geometry and electroconductivity of a scaffold greatly influence the spatial distribution of an electrical field (EF) when ES is applied.[93] In this section, we simulated the EF distribution on all coating combinations tested to better understand the influence of the PEDOT:PSS coating on the obtained EF. The electroconductivities of the materials used for the simulations are summarized in Table S1 (ESI†).

The first step was to determine a simpler modelling configuration that better describes the behavior of the filaments used to manufacture our scaffolds (Fig. S5, ESI†). Two configurations were envisaged: (a) the presence of a thin electroconductive PEDOT:PSS layer on top of an insulating material or (b) considering the whole filament to have the same electroconductivity as the PEDOT:PSS layer. The single 2D filament model reveals no predictable differences in the surrounding medium electrical field. Based on these results, the filament fibers that compose the orthogonal scaffold at the single well 3D model were parameterized as a single material loaded with each coating's electrical properties (configuration b).

The next step was to evaluate the influence of the PEDOT:PSS coatings on electrical field (EF) distribution around the whole scaffold. To do this, we measured, experimentally, the consequences of the application of a defined stimulation protocol (1.2 V) to osteogenic medium and using the same 6-well plate direct coupled stimulation setup for the electrical stimulation studies. We measured a peak of electric current of 0.067 A, followed by a sudden current drop that stabilizes around 0.001 A. With these currents, the model of a single well was computed to find the predicted EF of each coating material, and the results are shown in Table 5 and Fig. S6 (ESI†). We observed minimal changes on EF volumetric distribution when we compared the influence of the different coatings tested in our study (Fig. S5, ESI†). As such, we focused our analysis on the comparison between PCL (insulating) and DVS(NaOH)-Gel (electroconductive) samples.

Fig. 8 and Table 5 summarize the obtained results on the distribution of the applied electrical field on PCL and

Table 5 Simulated electrical field (EF) values in V m^{-1} for each of the coatings tested for 2 stimulation values: peak-value (1.2 V or 0.067 A) (ionic conductivity of the osteogenic media simulated was 0.01741 S cm^{-1})

Scaffolds		PCL/PCL(NaOH)	GOPS	GOPS(NaOH)	GOPS(NaOH)-Gel.	DVS	DVS(NaOH)	DVS(NaOH)-Gel.
0.067 A	EF (average)	312.45	34.352	74.40	13.004	29.14	39.96	22.56
	EF (maximum)	1648.50	304.25	550.77	138.57	269.52	338.40	220.73
	EF (minimum)	0.63	0.08	0.81	0.038	0.08	0.25	0.04

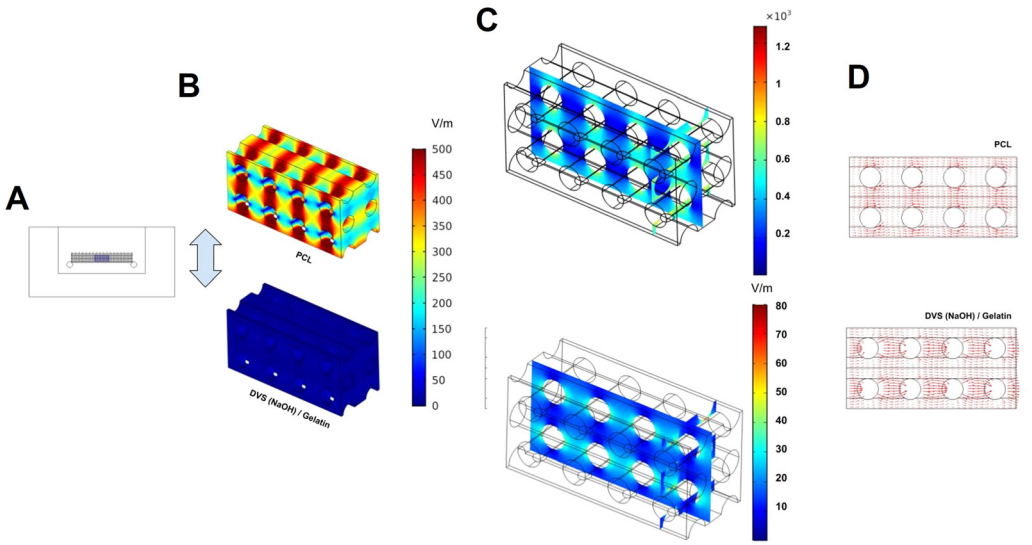

Fig. 8 Main results for the FEA of PCL and DVS(NaOH)-Gelatin. (A) Side-view of the scaffold area analyzed. (B) Predicted electrical fields around the volume analyzed and (C) the middle transversal area of the scaffold. (D) Predictive electrical field distribution model.

DVS(NaOH)-Gel samples. We observed higher field amplitudes (EF (maximum) − EF (minimum)) on the PCL sample, independently of the simulated current. A visual analysis to the obtained heat map of PCL (Fig. 8(B)) shows that this arises from heterogeneous electrical field distribution throughout the scaffold. We hypothesize that this is caused by scaffold geometry that creates natural obstacles that oppose liquid flow and charge dispersion. In sample DVS(NaOH)-Gel, such a phenomenon is not observed unless a finer scale is used (Fig. 8(C)).

Our results demonstrate that the presence of the PEDOT:PSS coating can ease charge movement throughout the whole scaffold and generate a more homogeneous EF when external ES is applied (Fig. 8(D)). We expect that this will allow a more homogeneous stimulation of cultured cells and avoid the formation of faradaic products, such as radical oxygen species (ROS), due to high intensity electrical fields. ROS formation is possible when a high EF (10 V cm^{-1}) is used for ES and can have beneficial effects on cardiac cell differentiation[94] and even lung cancer cell treatment.[95] Similar or even higher EF values are observed for our pristine PCL sample, increasing the potential of ROS formation with ES. For bone TE strategies, ROS formation has mixed effects on bone health. Some studies claim that ROS formation should ideally be minimized due to its negative impact on osteoblast viability and differentiation, and enhancement of osteoclast differentiation and activity.[96,97]

3.3. Electrical stimulation of MSCs during osteogenic differentiation

Our FEA results indicate that PCL-PEDOT:PSS scaffolds show clear advantages over pristine PCL scaffolds regarding EF distribution. Sample DVS(NaOH)-Gel shows chemical stability of the electroconductive coating for up to 21 days, favorable mechanical properties, and *in vitro* mineralization profile, and allows high MSC adhesion and colonization of the scaffold. As such, we decided to use sample DVS(NaOH)-Gel to perform ES studies during the osteogenic differentiation of MSCs. To assess the combined effect of the ES and conductive scaffolds, ES was also performed on PCL(NaOH) scaffolds as non-stimulated scaffolds (DVS(NaOH)-Gel and PCL(NaOH)) were also used as controls.

The metabolic activity of MSCs cultured under osteogenic induction conditions in DVS(NaOH)-Gel and PCL(NaOH) scaffolds with(ESTIM)/without(NO STIM) ES was monitored for 21 days (Fig. 9(A)). For all the conditions, the metabolic activity increased overtime throughout the 21 days of osteogenic differentiation. A lower cell metabolic activity was observed for the conductive DVS(NaOH)-Gel scaffolds in comparison to the non-

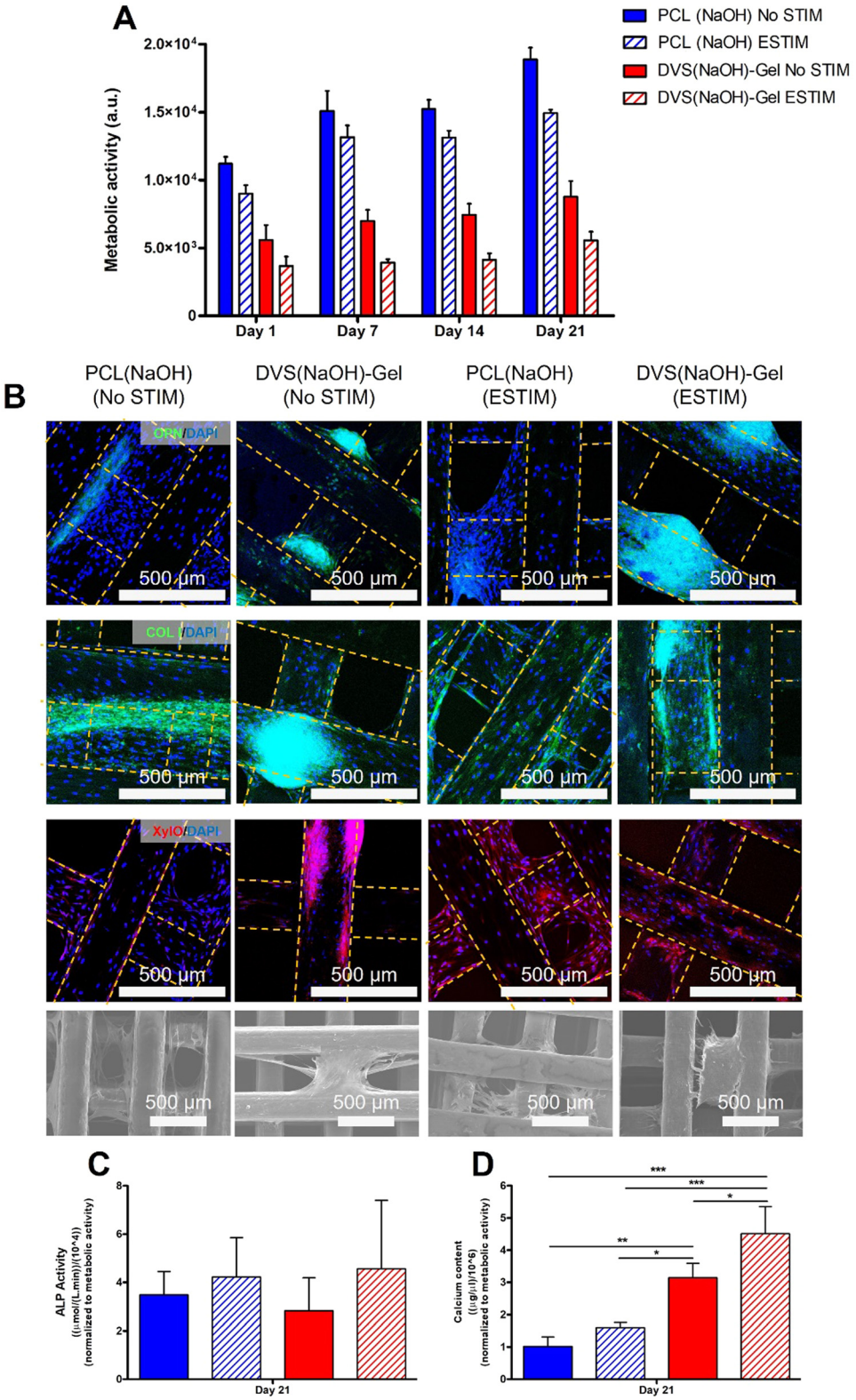

Fig. 9 Evaluation of the osteogenic differentiation of MSCs cultured on PCL(NaOH) and DVS(NaOH)-Gel scaffolds without (No STIM) or with electrical stimulation (ESTIM) for 21 days. (A) Metabolic activity was evaluated throughout the 21 days of culture (n = 6). (B) After 21 days of osteogenic differentiation, cells were stained for different bone-specific markers (Osteopontin – OPN, and Collagen I – COL I) and counter-stained with DAPI. Xylenol Orange (XylO) fluorescence staining was performed to assess calcium deposits and SEM images for whole cell morphology. (C) Quantification of ALP activity. (D) Quantification of calcium content, normalized to cell metabolic activity at day 21 (n = 3, * means $p < 0.05$, ** means $p < 0.01$ and *** means $p < 0.001$).

conductive PCL(NaOH) scaffolds. A similar trend was observed by Abedi and colleagues,[98] which reported lower cell metabolic activities in conductive chitosan/polyvinyl alcohol/MWCNTS in comparison to the chitosan/polyvinyl alcohol counterparts. For both scaffold conditions, ESTIM leads to a decrease in the metabolic activity of MSCs, which is concordant with results from previous ES studies performed by other authors using dental pulp stem cells[99] and BM-MSCs cultured on 3D collagen type I scaffolds.[100] In our previous study about the development of ECM-decorated scaffolds for bone TE, we observed lower cell metabolic activities during MSC osteogenic differentiation, and this did not affect the cells' osteogenic potential.[26] Moreover, application of ES has been shown to slow down neural cell proliferation while improving their differentiation.[101]

The main focus of this work was to develop 3D extruded conductive scaffolds and combine them with ES to promote the osteogenic differentiation of MSCs envisaging bone TE applications. At the end of the ES experiment, samples for the four different experimental conditions were obtained and evaluated towards production of bone ECM proteins and minerals (Fig. 9(B)–(D)), and also expression of bone-specific marker genes (Fig. 10).

3.3.1. Immunofluorescence analysis of bone-specific proteins. The main results for the morphological and immunofluorescence analysis of hBM-MSCs after osteogenic differentiation are summarized in Fig. 9(B). These include the staining of bone-specific proteins OPN and COL I (first 2 rows), xylenol orange staining (third row) to assess mineral deposition and complementary SEM images (fourth row) allowing the observation of cell morphology and distribution throughout the scaffolds. Our results evidence a clearly enhanced OPN expression in DVS(NaOH)-Gel scaffolds both without and with ES. The OPN staining in sample DVS(NaOH)-Gel (ESTIM) appears to be more intense than in sample DVS(NaOH)-Gel (No STIM). Such a trend was not observed for PCL(NaOH) scaffolds (ESTIM *vs.* No STIM). For COL I, we observed positive staining for all scaffolds tested, but the highest intensity was observed in both samples DVS(NaOH)-Gel regardless of the application of ES. Overall, these results suggest a positive effect of scaffold electroconductivity on MSC osteogenic differentiation. The increased fluorescence intensity of COL I suggests that the conductive DVS(NaOH)-Gel scaffolds support collagen production by MSCs for both No STIM and ESTIM conditions, which is concordant with the results reported by Hardy and colleagues using 3D conductive silk foam-based scaffolds.[102]

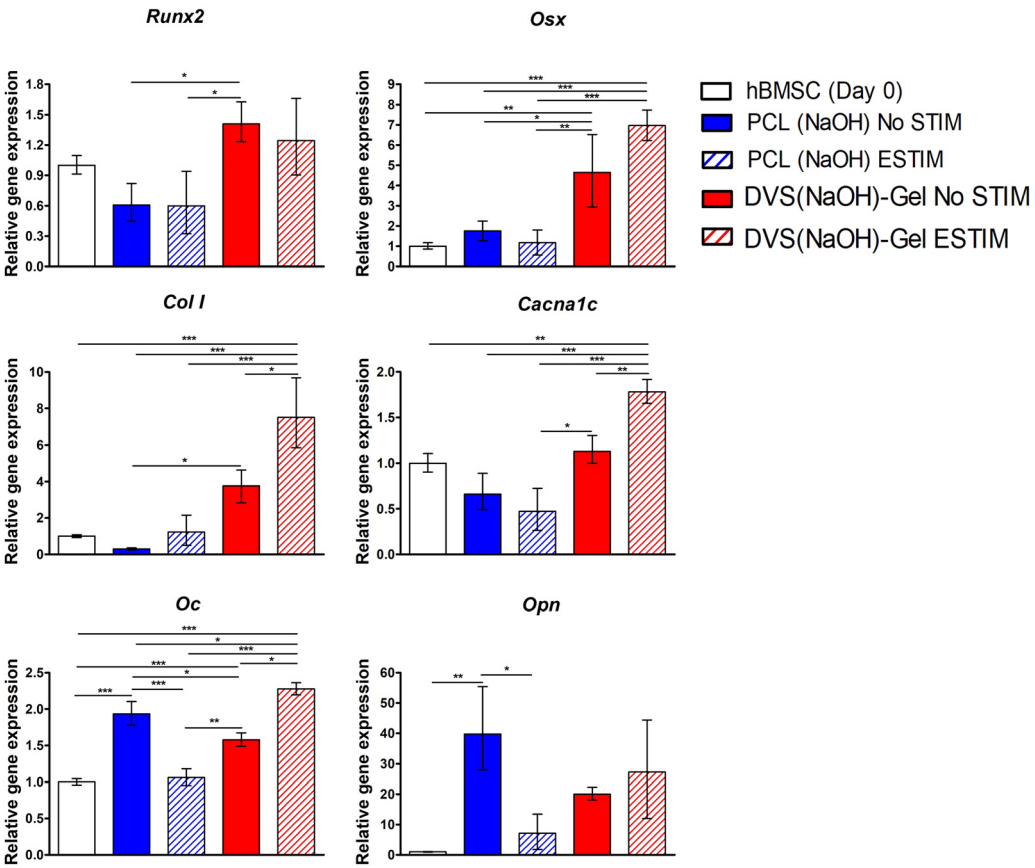

Fig. 10 Gene expression analysis by RT-qPCR after 21 days of MSC osteogenic differentiation on PCL(NaOH) and DVS(NaOH)-Gel scaffolds without (No STIM) or with electrical stimulation (ESTIM). Expressions of *Runx2*, *Osx*, *Col I*, *Cacna1c*, *Oc* and *Opn* were normalized to the endogenous gene *Gapdg* and calculated as a fold-change relative to the baseline expression of the control sample (MSCs before cell seeding at day 0). Results are presented as mean ± SD (n = 3, * means $p < 0.05$, ** means $p < 0.01$ and *** means $p < 0.001$).

The increased fluorescence intensity of OPN in samples DVS(NaOH)-Gel, especially for sample ESTIM, suggests that there is a synergy between ES and the conductive substrate to promote OPN expression. The presence of OPN indicates a more mature MSC osteogenic differentiation state, and the highest fluorescence intensity of OPN observed in DVS(NaOH)-Gel suggests an enhancement in MSC differentiation.

Xylenol orange staining images evidenced a more intense presence of mineral deposits in the conductive DVS(NaOH)-Gel scaffolds when compared to PCL(NaOH) scaffolds. When ES was applied, both scaffold types showed a much more intense and well-distributed mineral deposition, suggesting an important role of ES in the enhancement of tissue mineralization by differentiating MSCs. This is in agreement with what was observed in a recent study by Dixon & Gomulion,[103] which showed an improved mineralization (assessed by xylenol orange staining) after culturing MC3T3-E1 pre-osteoblasts in conductive PLA scaffolds exposed to ES when compared to non-conductive PLA scaffolds both with and without ES.

Overall, our immunostaining and xylenol orange staining results suggest that our electroconductive scaffold DVS(NaOH)-Gel provides a better support for MSC osteogenic differentiation. When ES is applied, the presence of terminal differentiation marker OPN and calcium deposition increase. To further confirm these results, quantitative assays were performed.

3.3.2. ALP activity and calcium deposition. ALP activity was evaluated, and the results are summarized in Fig. 9(C). The obtained results suggest a positive role of ES in promoting the ALP activity for both scaffolds, but the observed differences were not statistically significant. Similar (non-significant) enhancing effects of ES in ALP activity have been described in previous studies.[102,103] During MSC's osteogenic differentiation, ALP activity is enhanced as an early marker of osteogenesis,[104] reaching a peak around days 15–16.[105,106] Thus, at day 21 of osteogenic differentiation, we may observe a more mature osteoblast stage and thus the ALP levels will decrease. This observation is in accordance with previous studies reporting decreased ALP activities at day 21 in comparison to earlier time points.[107,108] Moreover, during the initial phases of the osteogenesis process, the mechanisms that regulate the ALP activity are highly complex comprising several interlaced signaling pathways (*e.g.* Wnt, FGF, and BMP2), the details of which are still poorly understood.[109]

The results from the calcium quantification assay performed after 21 days of osteogenic differentiation under the four different experimental conditions are presented in Fig. 9(D). Our results evidence the positive effect of ES on the calcium production by MSCs in both scaffold types; however, such an effect was only statistically significant when the cells were cultured on conductive scaffolds. This positive role of ES on MSC-based mineralization has been suggested to occur through the activation of the calcium-calmodulin pathway and by the upregulation of bone morphogenetic proteins (BMPs) and transforming growth factor-β (TGF-β) expression.[8,110]

The DVS(NaOH)-Gel scaffolds presented significantly higher calcium amounts than the PCL(NaOH) counterparts (No STIM – 1.54 fold), even when ES was applied (ESTIM – 2.46 fold). These observations are concordant with the results from xylenol orange staining (Fig. 9(B)) and other studies in the literature that report an enhancement in calcium production when secreting-cells are cultured on electroconductive substrates.[102,103,111]

Notably, combining DVS(NaOH)-Gel with ES resulted in significantly higher calcium deposition (2.29 fold increase *vs.* DVS(NaOH)-Gel No STIM and 2.46 fold increase *vs.* PCL(NaOH) ESTIM). This synergistic effect between conductive scaffolds and ES in promoting calcium production by MSCs is supported by previous work in the literature. Chen and colleagues[112] reported an increase of calcium deposition by human adipose-derived stem cells on PEDOT:PSS/MWNT substrates after the application of ES (AC, 0.2 V, 0.01 Hz, total stimulation of 1–14 days, after chemical induction). Moreover, they observed a concomitant enhancement in osteogenic differentiation after two weeks of culture.

3.3.3. Osteogenic marker gene expression. qRT-PCR analysis was performed to assess bone-specific gene expression by cells after 21 days of osteogenic differentiation in 3D-extruded PCL(NaOH) and DVS(NaOH)-Gel scaffolds with and without ES (Fig. 10). *RUNX2* expression was the highest in DVS(NaOH)-Gel No STIM, followed by DVS(NaOH)-Gel ESTIM. For samples PCL(NaOH) ESTIM and No STIM, *RUNX2* expression decreased when compared with the control cells. *OSX* expressions in DVS(NaOH)-Gel scaffolds both with and without ES were significantly higher in comparison to those of both PCL(NaOH) ESTIM and No STIM, and control cells, but were not significantly different between them. *OPN* gene expression was upregulated under all experimental conditions, but no significant differences were observed as a result of the use of conductive scaffolds or ES exposure. Finally, we observed a statistically significant upregulation of genes *COL I*, *CACNA1C* and *OC* for sample DVS(NaOH)-Gel ESTIM, when compared to all other samples in this study, including non-stimulated DVS(NaOH)-Gel scaffolds. For sample DVS(NaOH)-Gel No STIM, there was a statistically significant upregulation of *COL I vs.* PCL(NaOH) No STIM, *OC vs.* PCL(NaOH) STIM, and *CACNA1C vs.* PCL(NaOH) ESTIM, but always lower when compared to that in DVS(NaOH)-Gel ESTIM. Finally, for sample PCL(NaOH) ESTIM, when compared to PCL(NaOH) No STIM, no major changes on *RUNX2*, *OSX*, *COL I* and *CACNA1C* were observed, whereas *OC* and *OPN* were downregulated. These data support our previous observations of synergy between scaffold electroconductivity and ES on enhancing the osteogenic differentiation of hBM-MSCs.

The initial steps of MSC's osteogenic commitment are regulated by the expression of transcription factors such as *RUNX2*, followed by *OSX* in a more advanced stage.[113] ES has been reported to activate different signaling pathways (*e.g.* BMP/Smad, calcium-calmodulin or MAPK pathways) that enhance the expression of osteogenic genes *RUNX2* and *OSX*.[114] Our results showed upregulation of *RUNX2* and *OSX* expression when the cells were differentiated in conductive DVS(NaOH)-Gel scaffolds, regardless of exposure to ES. These results suggest a predominant effect of the scaffold electroconductivity

in promoting the expression or the early osteogenic marker genes *RUNX2* and *OSX*. Nalesso and colleagues[115] reported similar observations using 3D printed PCL/Graphene scaffolds. *OPN* gene upregulation observed for all experimental groups suggests a mature state of the bone ECM secreted by differentiating hBM-MSCs. However, the effects of ES on *OPN* gene expression were opposite for non-conductive (downregulation in PCL(NaOH) STIM) and conductive scaffolds (upregulation (albeit non-significant) on DVS(NaOH)-Gel ESTIM). OPN has been associated with the regulation of several bone physiological processes such as collagen organization, calcification and angiogenesis. OPN has also been described as a regulator of the nucleation of calcium phosphate during mineralization, which might arise from its negatively charged motifs (*e.g.* aspartic acid residues) that have a high affinity to calcium adsorption.[116]

Intracellular calcium oscillations have also been shown to regulate ES-mediated MSC osteogenesis, since calcium ions are well-described second messengers involved in several cellular processes. As a response to membrane depolarization caused by ES, calcium ion channels, such as voltage-gated calcium channels (VGCC), can mediate the influx of calcium ions, which in turn might activate ERK1/2, one of the main effectors of the MAPK pathway.[114] The calcium ions inside the cell can also bind to the protein calmodulin, initiating the calcium-calmodulin signaling cascade. This pathway might be involved in the activation of the transcription factor *Osx*, which is known to regulate the expression of several osteogenic marker genes including *ALP*, *OC* and *OPN*.[117]

Our results identified clearly a synergistic effect of conductive scaffolds and ES in enhancing the osteogenic differentiation of hBM-MSCs, as demonstrated by the significant upregulation of *CACNA1C*, *COL I* and *OC* marker genes. In accordance with our results, Liu and colleagues[118] also reported that combining ES with conductive 3D-printed poly(propylene fumarate) scaffolds coated with CNTs significantly enhanced osteogenic gene expression in MC3T3 pre-osteoblasts. *CACNA1C* gene encodes for a subunit of L-type VGCC, which have been shown to play a role in the signaling cascade (*e.g.*, promote *RUNX2* and *OSX* expression) regulating human MSC osteogenic differentiation and calcium deposition.[119] In fact, a previous study by S. Camarero-Espinosa and colleagues[120] showed that blocking L-VGCC lead to the downregulation of bone-specific gene (*COL I*, *RUNX2*, and *OC*) expression, impairing hBM-MSC ostegenic differentiation. *COL I* and *OC* upregulation has been associated with enhanced bone mineralization.[120,121] Thus, the significant upregulation of *COL I* and *OC* gene expressions resulting from the combination of conductive scaffolds and ES is in accordance with the higher calcium contents (mineralization) observed before (Fig. 9(D)). Our results demonstrate the combined effect of conductive materials and ES as a strategy to enhance the osteogenic differentiation potential of hBM-MSCs towards improved bone TE strategies.

3.4. Final considerations and future directions

We demonstrate here an easy, reliable, and versatile method for the production of electroconductive 3D scaffolds of PEDOT:PSS and PCL. The scaffold architecture used here is an orthogonal pattern, already studied in previous works of our group.[22,26,122] This facilitated our analysis and allowed us to focus on the materials chemistry of our system and its *in vitro* performance. There are other possible methods to produce 3D-structured PEDOT:PSS scaffolds, including ice-templating[37] and extrusion of concentrated PEDOT:PSS solutions.[15] Our method is compatible with scaffolds produced with advanced additive manufacturing techniques, which allow a more precise fine-tuning of size, architecture, and porosity. Moreover, it requires a single annealing step for PEDOT:PSS and at a relatively low temperature.

The chemistry used for the production of the PCL-PEDOT:PSS scaffolds is simple to implement and versatile in its applications. For example, other polyesters widely used in 3D-extrusion (*e.g.* poly(lactic acid), poly(glycolic acid), poly(vinyl alcohol)) have similar chemical groups to PCL.[19] As such, we also hypothesize that our method is versatile enough to be used with other support polymers.

Gelatin immobilization was not essential for our scaffold design, as PEDOT:PSS can support cell adhesion and growth.[37,40] However, we observed slight improvements in calcium deposition and cell spreading as a consequence (Fig. 6 and 7), which we decided to harness for our final design. Overall, the different cross-linkers used in the PEDOT:PSS coating can be used to immobilize other bioactive cues, including inorganic (*e.g.* hydroxyapatite, bioglass) or organic ones (*e.g.* extracellular matrix or other proteinaceous components). Considering these scaffolds can be used as implants for different areas of the bone tissue (*e.g.* cortical bone, cancellous/trabecular bone, bone marrow, and growth plate), we believe such versatility will allow fine-tuning the biochemical properties of the applied PEDOT:PSS coating to specific tissue requirements and/or cell niches.

Biodegradation is an important factor to consider when designing scaffolds for bone tissue engineering. PCL is reported to slowly degrade under physiological conditions, which can be accelerated by the presence of cells and/or enzymes (*e.g.* lipase).[20,123] PEDOT:PSS cannot biodegrade under physiological conditions. However, due to its physicochemical properties, it can intimately interact with cells and be integrated into newly formed tissue without inducing inflammation and the formation of scar tissue.[124–126] We hypothesize that the PEDOT:PSS coating might slightly delay the degradation profile of PCL. Moreover, the inclusion of gelatin within the coating might facilitate substrate remodeling and help enzymes penetrate inside the PCL skeleton. Such a phenomenon will need to be evaluated using appropriate *in vivo* models to better understand the degradation kinetics of our scaffolds after implantation.

Since cancellous/trabecular bone is highly vascularized, future studies should also aim at understanding the neovascularization potential of our scaffolds. This is of particular interest for future application in therapeutics, as ES is described to also enhance tissue vascularization.[127] Future studies, whether *in vitro* (co-culture of hBM-MSCs and endothelial cells) or

in vivo (histological analysis after implantation), should be performed to study a potential synergy between ES and our scaffolds.

ES of hBM-MSCs undergoing osteogenic differentiation on conductive scaffolds greatly enhanced the deposition of cell-secreted calcium and improved the differentiation profile. This is in accordance with current literature.[128] Nevertheless, few ES studies for BTE applications were conducted in combination with support electroconductive materials.[10,129] PEDOT:PSS and other electroconductive materials possess delocalized charges that can promote ion adsorption and induce mineral deposition, and therefore can be advantageous for BTE applications. We found that both ES and PEDOT:PSS based scaffolds can synergically improve cell-secreted calcium deposition while accelerating osteogenic differentiation (upregulation of *COL I*, *OC* and *CACNA1C* genes, accompanied by an increase in the expression of proteins OPN and COL I). Our results underlay the positive effect of combining electroconductive support materials and ES towards more efficient BTE strategies. These can potentially be used for studying the effect of ES as a therapeutic option to treat non-union fractures or to revert the progression of bone diseases, *e.g.* osteoporosis.

4. Conclusions

In this work, we successfully developed a method for producing electroconductive and stable PCL-PEDOT:PSS scaffolds for bone tissue engineering under ES. We were successful in anchoring different PEDOT:PSS coatings to alkaline-treated 3D-extruded PCL scaffolds. The obtained scaffolds were stable, had appropriate mechanical properties and facilitated *in vitro* calcium deposition. hBM-MSC adhesion and proliferation were further improved with the immobilization of gelatin within the PEDOT:PSS coating. The combination of ES with our 3D-extruded scaffolds improved the osteogenic differentiation of hBM-MSCs. This was shown through higher expression of *COL I*, *OC* and *CACNA1C*, and calcium deposition. We believe that this simple, reliable and versatile strategy can be employed in the future for the production of electroconductive scaffolds for bone tissue engineering without the need for complex equipment.

Author contributions

Conceptualization: J. C. S. and F. F. F. G. Supervision: J. C. S. and F. F. F. G. Project administration: J. C. S. and F. F. F. G. Methodology, investigation and validation: J. C. S. (cell culture and analysis), P. M. (3D-printing, sample production, mechanical tests, and MicroCT), J. Me. (FEA analysis), F. B. (mineralization assay), C. M. (mechanical tests), ACM (FTIR), N. A. (mechanical tests and FEA analysis), P. P.-F. (mechanical tests and FEA analysis), and FFFG (sample production, physicochemical analysis, SEM, stability assay and sample analysis, and cell sample analysis). Formal analysis: J. C. S., P. M., J. Me., P. P.-F., N. A., J. M. and F. F. F. G. Data curation and visualization: J. C. S. and F. F. F. G. Funding acquisition and resources: J. C. S., A. C. M., J. M. S. C., P. P.-F., N. A., J. M., F. C. F., and F. F. F. G. Writing – original draft: J. C. S. and F. F. F. G. Writing – review and editing: J. C. S., P. M., J. Me., F. B., C. M., A. C. M., J. M. S. C., P. P.-F., N. A., J. M., F. C. F. and F. F. F. G.

Conflicts of interest

The authors declare no financial/commercial conflicts of interests related to this work.

Acknowledgements

The authors acknowledge dedicated funding from Fundação para a Ciência e a Tecnologia (FCT) through projects BioMaterARISES (EXPL/CTM-CTM/0995/2021) and InSilico4OCReg (PTDC/EME-SIS/0838/2021). The authors also acknowledge funding provided by FCT through IT (UIDB/50008/2020), iBB (UID/BIO/04565/2022), Laboratório-Associado I4HB (LA/P/0140/2020), CDRSP (UIDB/04044/2020 and UIDP/04044/2020), CERENA (UIDB/04028/2020), project OptiBioScaffold (PTDC/EME-SIS/4446/2020), InnovaBIOMAS (2022.10564.PTDC), Associate Laboratory ARISE LA/P/0112/2020, and PhD scholarships 2021.05145.BD (awarded to JMe) and 2022.10572.BD (awarded to FB).

References

1 J. A. Kanis, N. Norton, N. C. Harvey, T. Jacobson, H. Johansson, M. Lorentzon, E. V. McCloskey, C. Willers and F. Borgström, *Arch. Osteoporosis*, 2021, **16**, 82.
2 J. Barnsley, G. Buckland, P. Chan, A. Ong, A. Ramos, M. Baxter, F. Laskou, E. Dennison, C. Cooper and H. Patel, *Aging Clin. Exp. Res.*, 2021, **33**, 759–773.
3 I. R. Reid and B.-E. Lancet, *Lancet*, 2022, **399**, 1080–1092.
4 J. Barbosa, F. Paz and S. Braga, *J. Med. Chem.*, 2021, **64**, 1260–1282.
5 M. Panteli, J. Vun, I. Pountos, A. Howard, E. Jones and P. Giannoudis, *J. Cell. Mol. Med.*, 2022, **26**, 601–623.
6 M. Griffin and B.-A. Eplasty, *Eplasty*, 2011, **11**, 303–353.
7 J. H. H. Fonseca, L. Bagne, D. H. Meneghetti, G. M. T. M. Dos Santos, M. A. M. A. Esquisatto, T. A. M. A. de Andrade, M. E. C. E. do Amaral, M. Felonato, G. F. Caetano, M. Santamaria and F. A. S. A. Mendonça, *J. Biomed. Mater. Res., Part B*, 2019, **107**, 924–932.
8 L. Leppik, H. Zhihua, S. Mobini, V. Parameswaran, M. Eischen-Loges, A. Slavici, J. Helbing, L. Pindur, K. Oliveira, M. Bhavsar, L. Hudak, D. Henrich and J. Barker, *Sci. Rep.*, 2018, **8**, 6307.
9 B. Oliveira, P. Berezikov, E.-L. Kynigopoulos, B. Han and L. Henrich, *Sci. Rep.*, 2019, **9**, 11433.
10 S. Meng, Z. Zhang and M. Rouabhia, *J. Bone Miner. Metab.*, 2011, **29**, 535–544.

11 J. Li, X. Liu, J. Crook and G. Wallace, *Mater. Sci. Eng., C*, 2020, **107**, 110312.
12 F. Sahm, V. Grote, J. Zimmermann, F. Haack, A. Uhrmacher, U. Rienen, R. Bader, R. Detsch and A. Jonitz-Heincke, *Front. Physiol.*, 2022, **13**, 965181.
13 T. Kreller, J. Zimmermann, U. Rienen, A. R. Boccaccini, A. Jonitz-Heincke and R. Detsch, *Biomater. Adv.*, 2023, **146**, 213285.
14 L. Moroni, J. Burdick, C. Highley, S. Lee, Y. Morimoto, S. Takeuchi and J. Yoo, *Nat. Rev. Mater.*, 2018, **3**, 21–37.
15 H. Yuk, B. Lu, S. Lin, K. Qu, J. Xu, J. Luo and X. Zhao, *Nat. Commun.*, 2020, **11**, 1604.
16 A. Youssef, S. Hollister and P. Dalton, *Biofabrication*, 2017, **9**, 012002.
17 C. Fernandes, C. Moura, R. M. Ascenso, S. Amado, N. Alves and P. Pascoal-Faria, *Design Engineering and Manufacturing*, 2020.
18 R. Watanabe, A. Matsugaki, O. Gokcekaya, R. Ozasa, T. Matsumoto, H. Takahashi, H. Yasui and T. Nakano, *Biomater. Adv.*, 2023, 213633in press.
19 Z. Arif, M. Khalid, R. Noroozi, A. Sadeghianmaryan, M. Jalalvand and M. Hossain, *Int. J. Biol. Macromol.*, 2022, **218**, 930–968.
20 F. F. Garrudo, D. E. S. E. Nogueira, C. A. V. A. Rodrigues, F. A. A. Ferreira, P. Paradiso, R. Colaço, A. C. Marques, J. M. S. M. Cabral, J. Morgado, R. J. Linhardt and F. C. Ferreira, *Biomater. Sci.*, 2021, **9**, 5359–5382.
21 J. Silva, C. Moura, N. Alves, J. Cabral and F. Ferreira, *Procedia Manuf.*, 2017, **12**, 132–140.
22 C. Moura, J. Silva, S. Faria, P. Fernandes, C. Silva, J. Cabral, R. Linhardt, P. Bártolo and F. Ferreira, *J. Biosci. Bioeng.*, 2020, **129**, 756–764.
23 M. Chi, N. Li, J. Cui, S. Karlin, N. Rohr, N. Sharma and F. Thieringer, *Front. Bioeng. Biotechnol.*, 2022, **10**, 989729.
24 M. Yoshida, P. Turner, C. McAdam, M. Ali and J. Cabral, *Biopolymers*, 2022, **113**, e23482.
25 C. Piard, H. Baker, T. Kamalitdinov and J. Fisher, *Biofabrication*, 2019, **11**, 025013.
26 J. Silva, M. Carvalho, R. Udangawa, C. Moura, J. Cabral, C. Silva, F. Ferreira, D. Vashishth and R. Linhardt, *J. Biomed. Mater. Res., Part B*, 2020, **108**, 2153–2166.
27 Y. Hsiao, C. Kuo and P. Chen, *Adv. Funct. Mater.*, 2013, **23**, 4649–4656.
28 C. Chen, X. Bai, Y. Ding and I.-S. Lee, *Biomater. Res.*, 2019, **23**, 25.
29 L. Cui, J. Zhang, J. Zou, X. Yang, H. Guo, H. Tian, P. Zhang, Y. Wang, N. Zhang, X. Zhuang, Z. Li, J. Ding and X. Chen, *Biomaterials*, 2019, **230**, 119617.
30 B. Lu, H. Yuk, S. Lin, N. Jian, K. Qu, J. Xu and X. Zhao, *Nat. Commun.*, 2019, **10**, 1043.
31 A. Wibowo, C. Vyas, G. Cooper, F. Qulub, R. Suratman, A. Mahyuddin, T. Dirgantara and P. Bartolo, *Materials*, 2020, **13**, 512.
32 E. Silva, B. Huang, J. Helaehil, P. Nalesso, L. Bagne, M. Oliveira, G. Albiazetti, A. Aldalbahi, M. El-Newehy, M. Santamaria-Jr, F. Mendonça, P. Bártolo and G. Caetano, *Bio-Des. Manuf.*, 2021, **4**, 190–202.
33 S. Biscaia, J. Silva, C. Moura, T. Viana, A. Tojeira, G. Mitchell, P. Pascoal-Faria, F. Ferreira and N. Alves, *Polymers*, 2022, **14**, 1669.
34 F. F. Garrudo, G. Filippone, L. Resina, J. C. Silva, F. Barbosa, L. F. Ferreira, T. Esteves, A. Marques, J. Morgado and F. Ferreira, *Polymers*, 2023, **15**, 2760.
35 S. Jorge, A. Ablú, F. Garrudo, A. Galvão, L. Santos, J. Morgado and A. Charas, *Polymer*, 2023, 126196.
36 F. Barbosa, F. Garrudo, A. Marques, J. Cabral, J. Morgado, F. Ferreira and J. Silva, *Int. J. Mol. Sci.*, 2023, **24**, 13203.
37 A. Guex, J. Puetzer, A. Armgarth, E. Littmann, E. Stavrinidou, E. Giannelis, G. Malliaras and M. Stevens, *Acta Biomater.*, 2017, **62**, 91–101.
38 M. R. Kumar and M. S. Freund, *RSC Adv.*, 2015, **5**, 57318–57327.
39 A. Lari, T. Sun and N. Sultana, *J. Nanomater.*, 2016, **2016**, 1–12.
40 L. Sordini, F. Garrudo, C. Rodrigues, R. Linhardt, J. Cabral, F. Ferreira and J. Morgado, *Front. Bioeng. Biotechnol.*, 2021, **9**, 591838.
41 N. Li, J. Cui, M. Chi, F. Thieringer and N. Sharma, *Mater. Des.*, 2023, **234**, 112362.
42 T. Kokubo and H. Takadama, *Biomaterials*, 2006, **27**, 2907–2915.
43 M. Carvalho, L. Alves, I. Bogalho, J. Cabral and C. Silva, *Front. Cell Dev. Biol.*, 2021, **9**, 747521.
44 J. Meneses, J. Silva, S. Fernandes, A. Datta, F. Ferreira, C. Moura, S. Amado, N. Alves and P. Pascoal-Faria, *Polymers*, 2020, **12**, 940.
45 S. Bontapalle and S. Varughese, *Polym. Degrad. Stabil.*, 2020, **171**, 109025.
46 H. Shi, C. Liu, Q. Jiang and J. Xu, *Adv. Electron. Mater.*, 2015, **1**, 1500017.
47 S. Jorge, L. Santos, A. Galvão, J. Morgado and A. Charas, *Adv. Mater. Interfaces*, 2021, **8**, 2100517.
48 J. Che, Y. Xiao, X. Zhu, X. Sun, J. Che, Y. Xiao, X. Zhu and X. Sun, *Polym. Int.*, 2008, **57**, 750–755.
49 A. Harris, P. Molino, A. Paolini and G. Wallace, *Electrochim. Acta*, 2016, **197**, 99–106.
50 A. Håkansson, S. Han, S. Wang, J. Lu, S. Braun, M. Fahlman, M. Berggren, X. Crispin and S. Fabiano, *J. Polym. Sci., Part B: Polym. Phys.*, 2017, **55**, 814–820.
51 D. Mantione, I. Del Agua, W. Schaafsma, M. ElMahmoudy, I. Uguz, A. Sanchez-Sanchez, H. Sardon, B. Castro, G. G. Malliaras and D. Mecerreyes, *ACS Appl. Mater. Interfaces*, 2017, **9**, 18254–18262.
52 S. Krainer and U. Hirn, *Colloids Surf., A*, 2021, **619**, 126503.
53 M. Klicova, Z. Oulehlova, A. Klapstova, M. Hejda, M. Krejcik, O. Novak, J. Mullerova, J. Erben, J. Rosendorf, R. Palek, V. Liska, A. Fucikova, J. Chvojka, I. Zvercova and J. Horakova, *Mater. Des.*, 2022, **217**, 110661.
54 F. F. F. Garrudo, C. A. Chapman, P. R. Hoffman, R. W. Udangawa, J. C. Silva, P. E. Mikael, C. A. V. Rodrigues,

J. M. S. Cabral, J. M. F. Morgado, F. C. Ferreira and R. J. Linhardt, *Eur. Polym. J.*, 2019, **117**, 28–37.
55 F. Garrudo, P. Mikael, C. Rodrigues, R. Udangawa, P. Paradiso, C. Chapman, P. Hoffman, R. Colaço, J. Cabral, J. Morgado, R. Linhardt and F. Ferreira, *Mater. Sci. Eng., C*, 2021, **120**, 111680.
56 Z. Zhu, C. Liu, J. Xu, Q. Jiang, H. Shi and E. Liu, *Electron. Mater. Lett.*, 2016, **12**, 54–58.
57 D. Sridharan, A. Palaniappan, B. Blackstone, J. Dougherty, N. Kumar, P. Seshagiri, N. Sayed, H. Powell and M. Khan, *Mater. Sci. Eng., C*, 2021, **118**, 111354.
58 L. Ghasemi-Mobarakeh, M. Prabhakaran, M. Morshed, M.-H. Nasr-Esfahani and S. Ramakrishna, *Biomaterials*, 2008, **29**, 4532–4539.
59 I. Prasertsung, S. Kanokpanont, R. Mongkolnavin, C. S. Wong, J. Panpranot and S. Damrongsakkul, *J. Biomater. Sci. Polym. Ed.*, 2012, **23**, 1485–1504.
60 I. Prasertsung, S. Kanokpanont, R. Mongkolnavin, C. S. Wong, J. Panpranot and S. Damrongsakkul, *Mater. Sci. Eng., C*, 2013, **33**, 4475–4479.
61 F. Barbosa, F. Ferreira and J. Silva, *Int. J. Mol. Sci.*, 2022, **23**, 2907.
62 T.-M. Huang, S. Batra, J. Hu, T. Miyoshi and M. Cakmak, *Polymer*, 2013, **54**, 6455–6462.
63 F. Furlani, E. Campodoni, N. Sangiorgi, M. Montesi, A. Sanson, M. Sandri and S. Panseri, *Int. J. Biol. Macromol.*, 2023, **224**, 266–280.
64 R. M. Silverstein, F. X. Webster and D. J. Kiemle, *Spectrometric identification of organic compounds*, John Wiley & Sons, Inc., 7th edition, 2005.
65 L. Wang, H. Meng, P. Shen, C. Bianchini, F. Vizza and Z. Wei, *Phys. Chem. Chem. Phys.*, 2010, **13**, 2667–2673.
66 N. Irfanita, I. Jaswir, M. Mirghani, S. Sukmasari, Y. Ardini and W. Lestari, *J. Phys.: Conf. Ser.*, 2017, **884**, 012090.
67 C. Moura, F. Ferreira and P. Bártolo, *Proc. CIRP*, 2016, **49**, 209–212.
68 M. Kim, C. Yun, E. Chalisserry, Y. Lee, H. Kang, S.-H. Park, W.-K. Jung, J. Oh and S. Nam, *Mater. Lett.*, 2018, **220**, 112–115.
69 W. Zhang, I. Ullah, L. Shi, Y. Zhang, H. Ou, J. Zhou, M. Ullah, X. Zhang and W. Li, *Mater. Des.*, 2019, **180**, 107946.
70 G. Renders, L. Mulder, L. Ruijven and T. Eijden, *J. Anat.*, 2007, **210**, 239–248.
71 V. Bousson, F. Peyrin, C. Bergot, M. Hausard, A. Sautet and J. Laredo, *J. Bone Miner. Res.*, 2004, **19**, 794–801.
72 Y. Yan, H. Chen, H. Zhang, C. Guo, K. Yang, K. Chen, R. Cheng, N. Qian, N. Sandler, Y. Zhang, H. Shen, J. Qi, W. Cui and L. Deng, *Biomaterials*, 2019, **190**, 97–110.
73 B. Huang, Y. Wang, C. Vyas and P. Bartolo, *Adv. Sci.*, 2022, 2203183.
74 O. Lindahl, *Acta Orthop. Scand.*, 1976, **47**, 11–19.
75 J. Xie, S. Zhong, B. Ma, F. Shuler and C. Lim, *Acta Biomater.*, 2013, **9**, 5698–5707.
76 E. Daskalakis, F. Liu, B. Huang, A. Acar, G. Cooper, A. Weightman, G. Blunn, B. Koç and P. Bartolo, *Int. J. Bioprint.*, 2021, **7**, 268.
77 A. Fallah, M. Altunbek, P. Bartolo, G. Cooper, A. Weightman, G. Blunn and B. Koc, *J. Mech. Behav. Biomed. Mater.*, 2022, **134**, 105418.
78 J. Ribeiro, S. Oliveira, J. Alves, A. Pedro, R. Reis, E. Fernandes and J. Mano, *Biofabrication*, 2017, **9**, 025015.
79 A. Olubamiji, Z. Izadifar, J. Si, D. Cooper, B. Eames and D. Chen, *Biofabrication*, 2016, **8**, 025020.
80 N. Alharbi, A. Daraei, H. Lee and M. Guthold, *Mater. Today Commun.*, 2023, **35**, 105773.
81 X. Wang, G. Feng, M. Li and M. Ge, *Polym. Bull.*, 2019, **76**, 2097–2111.
82 L. Kayser and D. Lipomi, *Adv. Mater.*, 2019, **31**, 1806133.
83 M. Murshed, *Cold Spring Harbor Perspect. Med.*, 2018, **8**, a031229.
84 X. Lin, S. Patil, Y.-G. Gao and A. Qian, *Front. Pharmacol.*, 2020, **11**, 757.
85 J. Park, V. Kaliannagounder, S. Jang, D. Yoon, A. Rezk, D. Bhattarai and C. Kim, *ACS Biomater. Sci. Eng.*, 2022, **8**, 1975–1986.
86 I. Rajzer, M. Rom, E. Menaszek, J. Fabia and R. Kwiatkowski, *Materials*, 2021, **14**, 4837.
87 X. Zhao, Y. Wu, Y. Du, X. Chen, B. Lei, Y. Xue and P. Ma, *J. Mater. Chem. B*, 2015, **3**, 3222–3233.
88 M. Jennings, I. Kendrick, C. Green and L.-S. Embark, *Embark*, 2018.
89 S. Atilgan, F. Yaman, U. Yilmaz, B. Görgün and G. Ünlü, *Biotechnol. Biotechnol. Equip.*, 2007, **21**, 205–210.
90 K. Maji, S. Dasgupta, B. Kundu and A. Bissoyi, *J. Biomater. Sci., Polym. Ed.*, 2015, **26**, 1190–1209.
91 W.-H. Lin, J. Yu, G. Chen and W.-B. Tsai, *Colloids Surf., B*, 2016, **138**, 26–31.
92 F. Papadogiannis, A. Batsali, M. Klontzas, M. Karabela, A. Georgopoulou, A. Mantalaris, N. Zafeiropoulos, M. Chatzinikolaidou and C. Pontikoglou, *Biomed. Mater.*, 2020, **15**, 064101.
93 J. Meneses, S. Fernandes, N. Alves, P. Pascoal-Faria and P. Miranda, *Effects of Scaffold Electrical Properties on Electric Field Delivery in Bioreactors*, 2021.
94 E. Serena, E. Figallo, N. Tandon, C. Cannizzaro, S. Gerecht, N. Elvassore and G. Vunjak-Novakovic, *Exp. Cell Res.*, 2009, **315**, 3611–3619.
95 K.-Y. Lo, S.-Y. Wu and Y.-S. Sun, *Microfluid. Nanofluid.*, 2016, **20**, 15.
96 M. Arai, Y. Shibata, K. Pugdee, Y. Abiko and Y. Ogata, *IUBMB Life*, 2007, **59**, 27–33.
97 H. Tao, G. Ge, X. Liang, W. Zhang, H. Sun, M. Li and D. Geng, *Acta Biochim. Biophys. Sin.*, 2020, **52**, 1055–1062.
98 A. Abedi, B. Bakhshandeh, A. Babaie, J. Mohammadnejad, S. Vahdat, R. Mombeiny, S. Moosavi, J. Amini and L. Tayebi, *Mater. Chem. Phys.*, 2021, **258**, 123842.
99 K. Oliveira, L. Leppik, K. Keswani, S. Rajeev, M. Bhavsar, D. Henrich and J. Barker, *Bioresearch Open Access*, 2020, **9**, 162–173.
100 B. Hiemer, M. Krogull, T. Bender, J. Ziebart, S. Krueger, R. Bader and A. Jonitz-Heincke, *Mol. Med. Rep.*, 2018, **18**, 2133–2141.

101 S. Wang, S. Guan, C. Sun, H. Liu, T. Liu and X. Ma, *Brain Res.*, 2023, **1798**, 148163.
102 J. G. Hardy, S. A. Geissler, D. Aguilar, M. K. Villancio-Wolter, D. J. Mouser, R. C. Sukhavasi, C. R. Cornelison, L. W. Tien, C. R. Preda, R. S. Hayden, J. K. Chow, L. Nguy, D. L. Kaplan and C. E. Schmidt, *Macromol. Biosci.*, 2015, **15**, 1490–1496.
103 D. Dixon and C. Gomillion, *J. Biomed. Mater. Res., Part B*, 2023, **111**, 1351–1364.
104 J. E. Aubin, *Rev. Endocr. Metab. Disord.*, 2001, **2**, 81–94.
105 Y. Zhang, V. Reddy, S. Wong, X. Li, B. Su, S. Ramakrishna and C. Lim, *Tissue Eng., Part A*, 2010, **16**, 1949–1960.
106 G. Vozzi, C. Corallo, S. Carta, M. Fortina, F. Gattazzo, M. Galletti and N. Giordano, *J. Biomed. Mater. Res., Part A*, 2014, **102**, 1415–1421.
107 M. Carvalho, J. Silva, R. Udangawa, J. Cabral, F. Ferreira, C. Silva, R. Linhardt and D. Vashishth, *Mater. Sci. Eng., C*, 2019, **99**, 479–490.
108 P. Alamán-Díez, E. García-Gareta, M. Arruebo and M. Pérez, *J. Biomed. Mater. Res., Part A*, 2023, **111**, 88–105.
109 S. Vimalraj, *Gene*, 2020, **754**, 144855.
110 I. Aleem, I. Aleem, N. Evaniew, J. Busse, M. Yaszemski, A. Agarwal, T. Einhorn and M. Bhandari, *Sci. Rep.*, 2016, **6**, 31724.
111 A. Shaabani, R. Sedghi, H. Motasadizadeh and R. Dinarvand, *Chem. Eng. J.*, 2021, **411**, 128449.
112 F.-J. Chen, Y.-S. Hsiao, I.-H. Liao, C.-T. Liu, P.-I. Wu, C.-Y. Lin, N.-C. Cheng and J. Yu, *J. Mater. Chem. B*, 2021, **9**, 7674–7685.
113 K. Nakashima, X. Zhou, G. Kunkel, Z. Zhang, J. Deng, R. Behringer and B. Crombrugghe, *Cell*, 2002, **108**, 17–29.
114 M. Guillot-Ferriols, S. Lanceros-Méndez, J. L. Ribelles and G. G. Ferrer, *Biomater. Adv.*, 2022, **138**, 212918.
115 P. Nalesso, W. Wang, Y. Hou, L. Bagne, A. Pereira, J. Helaehil, T. Andrade, G. Chiarotto, P. Bártolo and G. Caetano, *Bioprinting*, 2021, **24**, e00164.
116 A. BOSKEY, *Ann. N. Y. Acad. Sci.*, 1995, **760**, 249–256.
117 Y. Choi, J.-H. Choi, J.-W. Oh and K.-Y. Lee, *Biochem. Biophys. Res. Commun.*, 2013, **432**, 248–255.
118 X. Liu, M. George, S. Park, A. Miller, B. Gaihre, L. Li, B. Waletzki, A. Terzic, M. Yaszemski and L. Lu, *Acta Biomater.*, 2020, **111**, 129–140.
119 W. Jing, Y. Huang, P. Wei, Q. Cai, X. Yang and W. Zhong, *J. Biomed. Mater. Res., Part A*, 2019, **107**, 1443–1454.
120 S. Camarero-Espinosa and L. Moroni, *Nat. Commun.*, 2021, **12**, 1031.
121 M. Zoch, T. Clemens and R. Riddle, *Bone*, 2016, **82**, 42–49.
122 C. Moura, C. Silva, P. Bártolo and F. Ferreira, *Procedia Eng.*, 2015, **110**, 122–127.
123 E. Ozsagiroglu, B. İyisan and Y. Guvenilir, *Ekoloji*, 2013, **22**, 90–96.
124 S.-C. Luo, E. Ali, N. Tansil, H. Yu, S. Gao, E. Kantchev and J. Ying, *Langmuir*, 2008, **24**, 8071–8077.
125 N. Alba, Z. Du, K. Catt, T. Kozai and X. Cui, *Biosensors*, 2015, **5**, 618–646.
126 N. Fani, M. Hajinasrollah, M. H. A. Vostikolaee, M. B. Eslaminejad, F. Mashhadiabbas, N. Tongas, M. Rasoulianboroujeni, A. Yadegari, K. F. Ede, M. Tahriri and L. Tayebi, *J. Bioact. Compat. Polym.*, 2019, **34**, 436–441.
127 Y. Wang and X. Meng, *Regen. Ther.*, 2023, **24**, 237–244.
128 L. Leppik, K. Oliveira, M. Bhavsar and J. Barker, *Eur. J. Trauma Emerg. Surg.*, 2020, **46**, 231–244.
129 R. Silva, R. Xue, S. Torresi and S. Cartmell, *Biointerphases*, 2022, **17**, 011001.

